Geochemistry, Geophysics, Geosystems®

RESEARCH ARTICLE
10.1029/2023GC011134

Characterizing the Complexity of Subduction Zone Flow With an Ensemble of Multiscale Global Convection Models

Samuel L. Goldberg[1,2] and **Adam F. Holt**[1]

[1]Department of Marine Geosciences, Rosenstiel School of Marine, Atmospheric, and Earth Sciences, University of Miami, Miami, FL, USA, [2]Frost Institute for Data Science and Computing, University of Miami, Miami, FL, USA

Key Points:

- We embed detailed representations of Earth's subduction zones within global convection models to predict mantle flow at subduction zones
- Some subduction zones conform to ideal models, with upper mantle flow coupled to downgoing slabs, while others deviate from this pattern
- Dislocation creep partially decouples upper mantle flow from slab motion, increasing the fraction of non-ideal flow

Supporting Information:

Supporting Information may be found in the online version of this article.

Correspondence to:

S. L. Goldberg,
sam.goldberg@earth.miami.edu

Citation:

Goldberg, S. L., & Holt, A. F. (2024). Characterizing the complexity of subduction zone flow with an ensemble of multiscale global convection models. *Geochemistry, Geophysics, Geosystems*, *25*, e2023GC011134. https://doi.org/10.1029/2023GC011134

Received 24 JULY 2023
Accepted 25 JAN 2024

Author Contribution:

Conceptualization: Adam F. Holt
Funding acquisition: Adam F. Holt
Investigation: Adam F. Holt
Project administration: Adam F. Holt
Supervision: Adam F. Holt
Writing – review & editing: Adam F. Holt

Abstract Subduction zones are fundamental features of Earth's mantle convection and plate tectonics, but mantle flow and pressure around slabs are poorly understood because of the lack of direct observational constraints on subsurface flow. To characterize the linkages between slabs and mantle flow, we integrate high-resolution representations of Earth's lithosphere and slabs into a suite of global mantle convection models to produce physically plausible present-day flow fields for Earth's mantle. We find that subduction zones containing wide, thick, and long slabs dominate regional mantle flow in the neighboring regions and this flow conforms to patterns predicted by simpler regional subduction models. These subduction zones, such as Kuril-Japan-Izu-Bonin-Mariana, feature prismatic poloidal flow coupled to the downgoing slab that rotates toward toroidal slab-parallel flow near the slab edge. However, other subduction zones, such as Sumatra, deviate from this pattern because of the competing influence of other slabs or longer-wavelength mantle flow, showing that upper mantle flow can link separate subduction zones and how flow at subduction zones is influenced by broader scale mantle flow. We find that the non-linear dislocation creep reduces the coupling between slab motion and asthenospheric flow and increases the occurrence of non-ideal flow, in line with inferences derived from seismological constraints on mantle anisotropy.

1. Introduction

The convective flow of the Earth's mantle drives plate tectonics, transports heat and mass from the depths to the surface, and sets Earth apart from most other rocky planets (Pekeris, 1935). The sinking of cold, dense lithospheric mantle from the surface into the mantle at subduction zones is one of the most important components of this system (Stern, 2002; White et al., 1970). The pull of sinking slabs on plates is a primary driver of plate tectonics and mantle convection (Forsyth & Uyeda, 1975), and their descent return material into the Earth's interior to complete the convective cycle. The negative buoyancy of descending slabs within the mantle is a key feature of the global convective system and drives regional-scale flow of the upper mantle near subduction zones. This regional flow is both driven by the downward slab motion and affects their descent into the mantle. It also affects, and is affected by, larger-scale mantle flow that is driven by other large and distant density anomalies in the mantle (e.g., Hager & O'Connell, 1978; Husson, 2012). Characterizing and quantifying this two-way coupling is critical to correctly understanding Earth's subduction zones in the context of global-scale mantle flow.

Conditions of flow and pressure within the mantle are impossible to directly measure below Earth's surface, yet they are two of the defining properties of mantle dynamics. Numerical models of mantle flow have long been used to bridge the gap between available geophysical observations and these unknowns (e.g., Hager & O'Connell, 1979, 1981; Ricard & Vigny, 1989). Many numerical modeling studies have included slabs as negative density anomalies, demonstrating the importance of subduction and slab pull to reproducing observable global plate motions, but do not contain slabs that are both connected to the subducting plate yet asymmetrically decoupled from the overriding plate, limiting their ability to capture mantle dynamics in the vicinity of subduction zones (e.g., Becker & O'Connell, 2001; Conrad & Lithgow-Bertelloni, 2002; Hager, 1984; Lithgow-Bertelloni & Richards, 1998; Ricard et al., 1993). Regional subduction modeling studies have explored flow at subduction zones in greater detail, characterizing the vigor and style of 3-D flow around and near slabs, but have generally focused on modeling subduction systems in isolation without global context (e.g., Dvorkin et al., 1993; Funiciello et al., 2004; Funiciello, Morra., et al., 2003; Kincaid & Griffiths, 2003; Piromallo et al., 2006; Stegman et al., 2006).

Recent studies have examined the effect of background mantle flow on subduction dynamics within regional models (Chertova et al., 2018; Ficini et al., 2017; Paczkowski, Thissen, et al., 2014), including flow generated by

other subduction zones (e.g., A. F. Holt et al., 2017; Jagoutz et al., 2015; Király et al., 2016). These modeling studies suggest that far-field mantle flow strongly influences subduction dynamics, but do not place these insights in a global and geographic context. Conversely, Hager and O'Connell (1978) and Husson (2012) use global models of mantle flow to suggest that slab dips and trench motions are controlled by long-wavelength mantle flow but do not include the regional effects of subduction on mantle flow in their simulations. A. F. Holt and Royden (2020) developed analytical flow models to target the coupling of slabs and broader scale mantle flow; they did incorporate slab effects on flow but assumed relatively simple upper mantle flow patterns and highly idealized slab shapes. Hence, although these various studies suggest strong interactions between regional subduction and global-scale flow, they fall short of capturing the full multi-scale coupling. Only a few studies (Alisic et al., 2010, 2012; Hu et al., 2022; Stadler et al., 2010) have combined both detailed realistic shorter-wavelength structure—namely high-resolution slabs that are decoupled from the overriding plate with thin, inclined weak zones that rest above and do not cut through the slab—with representations of Earth's long-wavelength mantle density structure, but they do not explicitly examine flow near subduction zones and its interactions with longer-wavelength mantle convection. Hence, while these studies have illuminated important insights into mantle convection and subduction, the patterns of subduction zone flow and pressure at depth remain poorly studied, especially the two-way coupling between regional subduction dynamics and long-wavelength mantle flow. Understanding the contribution of subduction to global mantle flow and, conversely, the influence of long-wavelength flow on subduction dynamics is critical for understanding Earth's mantle convective system.

In this study, we embed high-resolution representations of Earth's lithosphere and slabs, with weak slab-aligned plate boundaries, in Earth-like global models of mantle flow. We vary the mantle structure and mechanical properties of these models to produce an ensemble of self-consistent and physically plausible solutions for the three-dimensional velocity and dynamic pressure within the Earth's mantle. From this suite of models, we extract the upper mantle flow and pressure patterns adjacent to slabs to assess mantle flow around subduction zones and its interactions with global mantle dynamics and to identify the robust trends that emerge from an ensemble of different models. We find that subduction zones with large and thick slabs such as Kuril-Japan-Izu-Bonin-Mariana are largely independent of other mantle structures and are themselves primary drivers of longer-wavelength flow patterns; the dynamic pressure generated by the negatively buoyant slab drives regional flow that conforms broadly to the canonical view of subduction zone flow derived from previous 3-D models. In contrast, flow at subduction zones with less negatively buoyant slabs deviates from these trends and is more strongly influenced by longer-wavelength flow, including that associated with other subduction zones. We also explore the dependence of flow patterns and pressure gradients on mantle rheology, confirming previous studies showing that non-linear dislocation creep enhances and localizes flow in rapidly deforming regions such as around slab edges at subduction zones. We find that this effect weakens the coupling between slab motion and upper mantle flow, decreases along-strike pressure gradients under slabs, and facilitates non-idealized flow patterns. Our findings illustrate the complex connections between slab motion and mantle flow and provide a physical framework for how and why slabs variably drive large-scale flow or are themselves governed by it.

2. Materials and Methods

2.1. Numerical Approach

We ran global models of Earth's mantle convection using the ASPECT finite element code (version 2.4) to solve the Stokes equations for the flow of an incompressible viscous fluid and the conservation of energy for a material without internal or viscous heating (Bangerth et al., 2021a, 2021b; Heister et al., 2017; Kronbichler et al., 2012),

$$\nabla \cdot \mathbf{v} = 0, \tag{1}$$

$$-\nabla \cdot 2\eta\dot{\mathbf{e}} + \nabla p = \rho\mathbf{g}, \tag{2}$$

$$\rho C_p\left(\frac{\partial T}{\partial t} + \mathbf{v}\cdot\nabla T\right) - k\nabla^2 T = 0, \tag{3}$$

where $\mathbf{v}$ is the velocity, η is the viscosity, $\dot{\mathbf{e}}$ is the deviatoric strain rate tensor, p is the pressure, ρ is the fluid density, $\mathbf{g}$ is the gravitational acceleration, C_p is the specific heat capacity, T is the temperature, and k is the

Table 1
Model Parameters and Values/Ranges

Parameter	Definition	Value	Units
C_p	Specific heat capacity	1,250	J kg^{-1} K^{-1}
k	Thermal conductivity	4.7	W m^{-1} K^{-1}
ρ_{ref}	Reference mantle density	3,300	kg m^{-3}
ω	Shear wave velocity-density scaling	0.2	–
T_{ref}	Reference interior mantle temperature	1,573	K
T_{surf}	Surface temperature	273	K
α	Thermal expansivity	3×10^{-5}	K^{-1}
g	Gravitational acceleration	10	m s^{-2}
A_{diff}	Diffusion creep coefficient	4.25×10^{-11} to 1.275×10^{-10} (upper mantle) 2.41×10^{-13} to 1.45×10^{-12} (lower mantle)	$(Pa\ s)^{-1}$
A_{disl}	Dislocation creep coefficient (upper mantle only)	3.96×10^{-16} to 1.856×10^{-14}	$(Pa\ s)^{-n}$
E_{diff}	Diffusion creep activation energy	3×10^5	J
E_{disl}	Dislocation creep activation energy	5.4×10^5	J
V_{diff}	Diffusion creep activation volume	4×10^{-6} (upper mantle), 2.5×10^{-6} (lower mantle)	m^3
V_{disl}	Dislocation creep activation volume	1.2×10^{-5}	m^3
n	Dislocation creep stress exponent	3.5	–

thermal conductivity. These equations describe the conservation of mass, momentum, and energy, respectively. Values used for model parameters are given in Table 1.

The model domain consists of a spherical shell representing the Earth's mantle, with an inner radius of 3,471 km and an outer radius of 6,371 km. We used a spatially uniform gravitational acceleration of 10 m/s^2, pointing radially inwards. We imposed free slip boundary conditions at the inner and outer boundaries. We discretized this domain using ASPECT's spatially variable mesh refinement functionality to use locally higher resolution within the lithosphere, slabs, plate boundaries, and in regions with high viscosity gradients (Figure S1 in Supporting Information S1). The maximum cell spacing of ~80 km vertically and ~150 km laterally is found in the lower mantle, while the minimum cell spacing of ~5 km vertically and ~15 km laterally is found in the most highly refined regions. This approach results in ~8,000,000 cells unequally distributed throughout the model domain, with ~350,000,000 degrees of freedom. To capture the instantaneous flow resulting from Earth's present conditions, we ran the simulation for four timesteps using a time interval set adaptively using a maximum Courant number of 0.5; in practice, this resulted in timesteps of $\sim 10^4$ years. We performed all analyses on the solution following the second timestep. Given the typical flow velocities of <10 cm/yr, we did not observe significant advection of the mantle structure over the course of our simulations. We removed the net body rotation from the modeled velocity field, which does not affect the solution. Each simulation took ~5–20 hr wallclock time running on 960 cores (24 Skylake nodes) on the Stampede2 cluster at the Texas Advanced Computing Center.

2.2. Model Inputs

For the model initial condition, we constructed the thermal structure of the Earth's mantle from several geophysical data sets (Figure 1), guided in part by past studies (Alisic et al., 2010, 2012; Davies et al., 2019; Steinberger, 2016). For the ambient mantle thermal structure below 300 km depth, we estimated the temperature from global shear-wave velocity tomography models. For our reference model, we used the SAVANI shear wave velocity model (Auer et al., 2014) but also ran simulations using TX2019slab and SL2013sv (Lu et al., 2019; Schaeffer & Lebedev, 2015) (see "Suite of simulations" section, Tables 2 and 3 for details). We converted seismic velocity (v_s) to density (ρ) using the following scaling relation,

$$\frac{\rho - \rho_{ref}}{\rho_{ref}} = \omega \delta v_s, \quad (4)$$

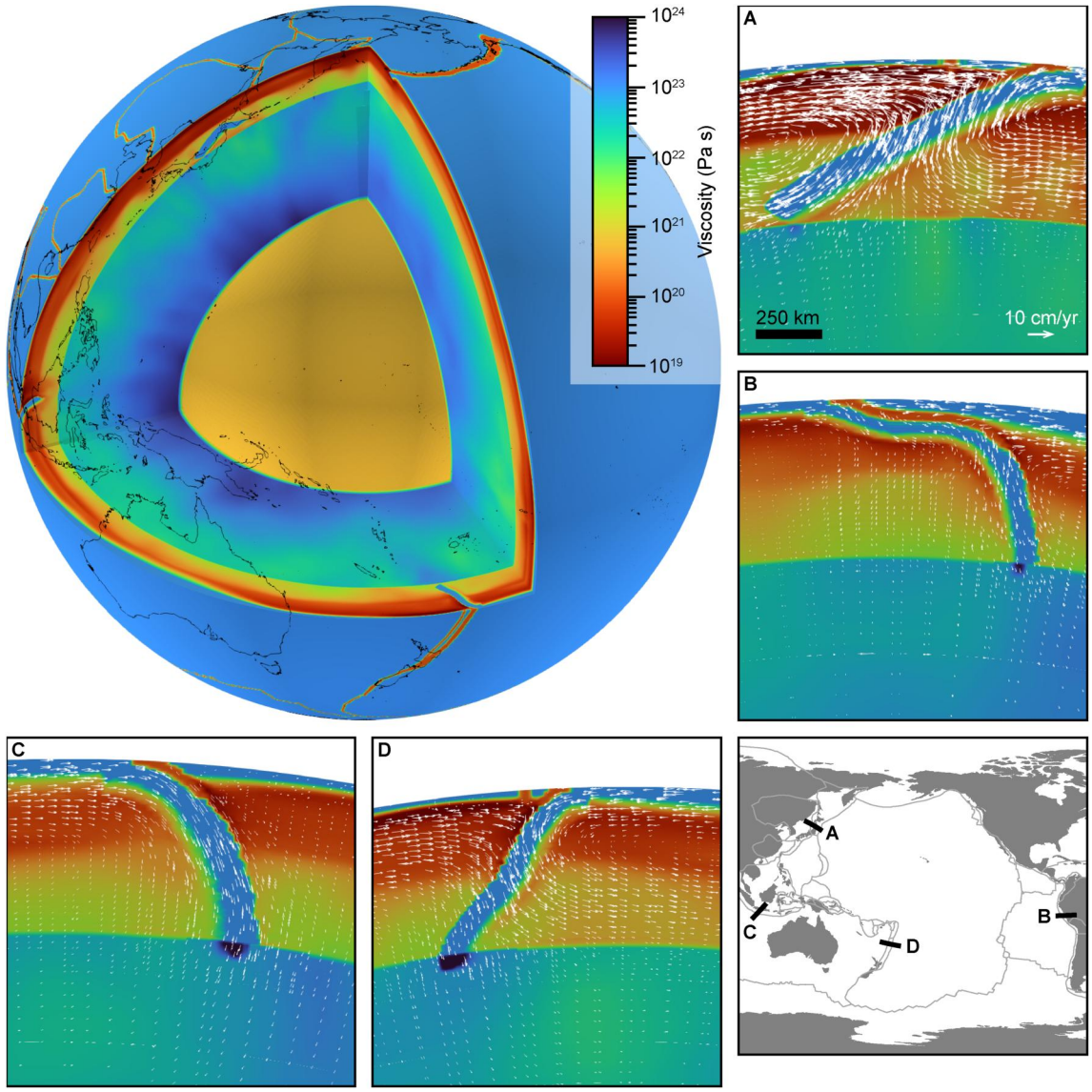

Figure 1. Cross section of the mantle model, colored by effective viscosity from our reference model. The viscosity represents the combined effects of temperature, pressure, and strain rate (e.g., high-viscosity slabs and lithosphere, low-viscosity rapidly straining asthenosphere) as well as weak plate boundaries. Panels (a–d) show slices through four representative subduction zones (Honshu Japan, South America, Sumatra, and Kermadec), with locations of slices shown on the locator map.

where ρ_{ref} is a reference average density for mantle rock and ω is a dimensionless scaling factor representing the effect of density variations on shear wave velocity anomalies. We use a constant value of 0.2 (e.g., Becker & Faccenna, 2011; Davies et al., 2019), thereby simplifying our models to neglect compositional and depth-dependent mineral physics effects. Values of all parameters are given in Table 1. We then converted density to temperature (T) using a linear thermal expansion law,

$$T = T_{\text{ref}} - \frac{1}{\alpha}\frac{\rho - \rho_{\text{ref}}}{\rho_{\text{ref}}}, \tag{5}$$

where T_{ref} is the reference interior mantle temperature and α is the coefficient of thermal expansion.

While we use shear-wave seismic tomography to reconstruct the deep mantle thermal structure, this simple scaling approach does not accurately reproduce the lithosphere and uppermost mantle due to the contaminating influence of compositional variations (Steinberger & Becker, 2018). We therefore do not use tomography for the

Table 2
List of Model Runs With Same Input Thermal Structure (See Methods) but Different Sets of Rheological Parameters

Model run	Reference viscosity at 330 km	Diffusion creep viscosity increase at 660 km	Lithosphere/slab viscosity	Plate boundary viscosity
1	1×10^{21}	10	10^{22}	10^{19}
2	1×10^{21}	10	10^{22}	10^{20}
3	1×10^{21}	10	10^{23}	10^{19}
4	1×10^{21}	10	10^{23}	10^{20}
5	1×10^{21}	10	10^{24}	10^{19}
6	1×10^{21}	10	10^{24}	10^{20}
7	2×10^{21}	10	10^{22}	10^{19}
8	2×10^{21}	10	10^{22}	10^{20}
9	2×10^{21}	10	10^{23}	10^{19}
10	2×10^{21}	10	10^{23}	10^{20}
11	2×10^{21}	10	10^{24}	10^{19}
12	2×10^{21}	10	10^{24}	10^{20}
13	3×10^{21}	20	10^{22}	10^{19}
14	3×10^{21}	20	10^{22}	10^{20}
15	3×10^{21}	20	10^{23}	10^{19}
16	3×10^{21}	20	10^{23}	10^{20}
17	3×10^{21}	20	10^{24}	10^{19}
18	3×10^{21}	20	10^{24}	10^{20}
19	2×10^{21} †	10	10^{22}	10^{19}
20	2×10^{21} †	10	10^{22}	10^{20}
21	2×10^{21} †	10	10^{23}	10^{19}
22	2×10^{21} †	10	10^{23}	10^{20}
23	2×10^{21} †	10	10^{24}	10^{19}
24	2×10^{21} †	10	10^{24}	10^{20}
25	1×10^{21} †	10	10^{23}	10^{20}
26	3×10^{21} †	20	10^{23}	10^{20}

Note. Run 10 (gray shading) is our reference model. Runs 19–26 (marked with †), do not include dislocation creep.

uppermost mantle; we smoothly transition from the tomographic structure described in Equations 4 and 5 at 350 km and below (linear weighting of 1) to no tomographic structure at 250 km and above (linear weighting of 0). At shallow depths, we instead model the thermal structure of the variable-thickness lithosphere using the lithospheric thickness model of Steinberger and Becker (2018) (their "mean_no_slabs" model), and assuming an error-function half-space cooling model (Turcotte & Schubert, 2014):

Table 3
List of Model Runs With the Same Rheology (Same as Reference Case Above) but Different Input Thermal Structures

Model run	Upper mantle tomography source	Lower mantle tomography source	Slab geometry
10 (reference)	SAVANI	SAVANI	Slab2
27	SL2013sv	SAVANI	Slab2
28	TX2019slab	TX2019slab	Slab2
29	SL2013sv	TX2019slab	Slab2
30	No tomography (slabs and lithosphere only)	SAVANI	Slab2
31	SAVANI	SAVANI	Slab2 + Japan slab "tail"

$$T(d) = T_{\text{ref}} + (T_{\text{surf}} - T_{\text{ref}})\,\text{erfc}\left(\frac{d}{0.8621D}\right), \tag{6}$$

where T_{surf} is the surface temperature, d is the depth below the surface, and D is the (geographically variable) depth of the base of the lithosphere. The coefficient 0.8621 is chosen such that the temperature at the base of the lithosphere is 90% of the difference between the surface and interior temperature, following Turcotte and Schubert (2014). We use this approach globally, without differentiation between continental and oceanic lithospheres. The Steinberger and Becker (2018) model, derived from seismic tomography, largely agrees with estimates of lithospheric thickness based on crustal age for oceanic lithosphere younger than 110 Ma, and is highly correlated with estimates from elastic thickness for both oceanic and continental lithospheres (Steinberger & Becker, 2018).

Most global tomography models also fail to reproduce slabs in detail due to their comparatively coarse resolution relative to the high temperature gradients expected in cold slabs. Moreover, slabs are generally poorly imaged by S relative to P waves (e.g., Lu et al., 2019). We therefore reconstructed three-dimensional slabs within the upper mantle using the Slab2 data set (Hayes et al., 2018), which contains gridded data sets of depth to slab top, strike, dip, and thickness for 27 globally distributed slabs. The Slab2 slab surfaces are constrained by a combination of Benioff zone seismicity and P-wave tomography; the thickness is estimated from the age of the subducting oceanic plate (Hayes et al., 2018). Although it does not capture the full depth extent of some slabs, it represents a conservative but widely used and reliable estimate of the geometry of subducted slabs within Earth's mantle. From these, we constructed the three-dimensional extent of each slab by extrapolating the thickness downwards from the slab top along the vector normal to the strike and dip at each point. Within the slab, we adopt slab-normal temperature profiles equivalent to those of the surface lithosphere. For points within the 3-D slab body, the calculated slab temperature replaced the temperature estimate from other sources (e.g., tomography). The contribution of each of these three components (tomography, lithosphere, slabs) can be seen in Figure 1. The buoyant stresses were again computed from the temperature field using a linear thermal expansion law (Equation 5).

2.3. Rheological Model

We used a composite viscous flow law that simulates both diffusion and dislocation creep of mantle material (Hirth & Kohlstedt, 2003; Karato & Wu, 1993). Our idealized diffusion creep viscosity is given by the expression

$$\eta_{\text{diff}} = \frac{1}{2} A_{\text{diff}}^{-1} \exp\left(\frac{E_{\text{diff}} + PV_{\text{diff}}}{RT}\right), \tag{7}$$

where A_{diff} is the diffusion creep coefficient (including the effect of grain size, held to be constant within the upper or lower mantle), E_{diff} is the diffusion creep activation energy, P is the pressure, V_{diff} is the diffusion creep activation volume, R is the ideal gas constant, and T is the temperature. Therefore, in our models, the diffusion creep viscosity depends only on temperature and pressure. In contrast, the dislocation creep viscosity also depends on the strain rate as a result of a non-linear viscous flow law. The effective viscosity of dislocation creep is given by the expression

$$\eta_{\text{disl}} = \frac{1}{2} A_{\text{disl}}^{-\frac{1}{n}} \dot{\epsilon}^{\frac{1-n}{n}} \exp\left(\frac{E_{\text{disl}} + PV_{\text{disl}}}{nRT}\right), \tag{8}$$

where A_{disl} is the dislocation creep coefficient (including the effect of grain size, held to be constant within the upper mantle), E_{disl} is the dislocation creep activation energy, P is the pressure, V_{disl} is the dislocation creep activation volume, $\dot{\epsilon}$ is the square root of the second invariant of the strain rate tensor, and n is the stress exponent from the power-law flow law. The effective viscosity is taken as the harmonic mean of the diffusion and dislocation creep effective viscosities,

$$\eta_{\text{eff}} = \left(\frac{1}{\eta_{\text{diff}}} + \frac{1}{\eta_{\text{disl}}}\right)^{-1}. \tag{9}$$

Although we model mantle material as incompressible, and thus without an adiabatic temperature gradient, the temperature values used in the viscosity calculations incorporate an adiabatic temperature gradient of 9.24×10^{-9} K/Pa to replicate the temperatures experienced by mantle material at depth.

We chose coefficients to match bulk constraints on upper-mantle viscosity from geophysical evidence such as glacial isostatic adjustment and long-wavelength geoid anomalies (Hager, 1984; Hager et al., 1985; Haskell, 1935; Lau et al., 2016; Mitrovica & Forte, 2004; Steinberger & Calderwood, 2006). We compute our coefficients for diffusion and dislocation creep to give chosen diffusion and dislocation creep viscosity at 330 km depth (middle of the upper mantle) at the reference ambient mantle temperature and a reference strain rate of 10^{-15} s^{-1} (see next section for details). We adopt this approach because of uncertainty in both the physical and mantle properties that factor into the coefficients (e.g., water content and grain size) and the uncertainty inherent in extrapolating experimentally derived coefficients to the low strain rates of mantle convection. We set the dislocation creep to be active only in the upper mantle, and impose a set viscosity increase (either 10- or 20-fold for the reference diffusion creep viscosity) at the upper-lower mantle boundary at 660 km depth by choosing the lower mantle diffusion creep coefficient appropriately. Because we choose the coefficient to match bulk constraints on mantle viscosity, the grain size is not an independent variable and is thus included in our coefficient. For other parameters, we used values consistent with dry diffusion and dislocation creep in olivine (Table 1) (Hirth & Kohlstedt, 2003).

The temperature dependencies in the flow laws produce very high viscosities in the cold lithosphere and slabs, which are likely reduced by other mechanisms of low-temperature deformation. Therefore, we impose upper mantle maximum viscosity, which effectively sets the strength of the lithosphere and slabs. Our reference model used a limit of 10^{23} Pa s; other simulations ranged from 10^{22} to 10^{24} Pa s (Table 2). This gives a viscosity contrast between slabs and asthenosphere of 10^{1} to 10^{4}. This range of viscosities, and the range of contrasts between the lithosphere and asthenosphere, bracket inferences from subduction zone topography and gravity (e.g., Billen & Gurnis, 2003, 2005; Moresi & Gurnis, 1996), slab shapes and strain rates (e.g., Čížková et al., 2002; W. E. Holt, 1995), and plate driving force considerations (e.g., Becker & Faccenna, 2009; Conrad & Hager, 1999; F. Funiciello et al., 2008; Wu et al., 2008). We also imposed a minimum viscosity of 10^{19} Pa s in the upper mantle. For the lower mantle, we set the minimum viscosity at 10^{20} Pa s and the maximum at 10^{24} Pa s.

In addition to the temperature- and strain rate-dependent viscosity described above, we impose 30 km-wide weak zones in the lithosphere with fixed viscosity along plate boundaries using the data set of Bird (2003). Our reference model uses a viscosity of 10^{20} Pa s; other simulations use 10^{19} Pa s (Table 2). For subduction zones, the plate boundary zone aligns with and sits on top of the slab top from Slab2 (Hayes et al., 2018); the 30-km width is slab-normal. For other boundaries, the weak zone is vertical, and the 30 km width is horizontal. Plate boundary zones extend to the base of the lithosphere. Since we are modeling complex visco-elasto-plastic deformation along plate boundaries as viscous deformation over a finite width, there is a tradeoff between the chosen viscosity and boundary width. Specifically, for a given stress across the plate boundary, the slip rate between adjacent plates will scale with the boundary width divided by the viscosity. As a result, neither the chosen width nor viscosity directly corresponds to a physically relevant parameter; their combined effect simulates the actual processes that enable slip between adjacent plates as viscous flow.

2.4. Model Simplifications

No numerical model can fully replicate the complexity of the natural world; we must necessarily make simplifying assumptions to render the problem tractable. We attempt to strike an appropriate balance between simplicity and complexity that captures the important physical processes by which mantle convection, plate tectonics, and subduction operate, such as temperature-dependent density and viscosity, diffusion and dislocation creep, and complex mantle thermal structure, without introducing unnecessary free parameters. Most of our constants are uniform with depth, such as the thermal expansivity, wavespeed-density scaling, and mantle reference temperature and density; we omit compressibility. While other studies have included depth-dependent forms of these parameters (e.g., Steinberger & Calderwood, 2006), detailed depth variability is difficult to constrain with observations and we do not expect these additional complexities to alter the first-order features of our predicted flow patterns. Our primary target of interest is upper-mantle flow, which is less sensitive to pressure-dependent effects than the lower mantle. For the same reason, we also chose not to incorporate compositional effects, instead representing the mantle as compositionally homogeneous, with variable properties due only to temperature and pressure (except for weak plate boundary zones).

2.5. Suite of Simulations

To assess the influence of rheology on upper mantle flow and subduction dynamics, we performed a suite of simulations varying several key rheological parameters around the values used in our reference model (Table 2) while using the same input thermal structure. Since these parameters are uncertain, we explored a plausible range for the Earth's mantle. We used three sets of diffusion and dislocation creep prefactors chosen to give diffusion and dislocation creep viscosities of 1, 2, and 3 × 10^{21} Pa s at 330 km depth at the reference ambient mantle temperature and a reference strain rate of 10^{-15} s^{-1}. At the 660-km boundary between the upper and lower mantle, our reference model features a 10-fold viscosity jump for the reference diffusion creep viscosity (i.e., at the reference temperature); some models feature a 20-fold jump (Table 2). The absolute viscosity values and the magnitude of the mid-mantle jump are consistent with mantle viscosity inferred from glacial isostatic adjustment, mantle convection, and the long-wavelength geoid (Hager, 1984; Hager et al., 1985; Haskell, 1935; Lau et al., 2016; Mitrovica & Forte, 2004; Steinberger & Calderwood, 2006). In addition to this variation in the ambient viscosity profile, we also vary the slab and lithosphere viscosities by setting the maximum upper-mantle viscosity to 10^{22}, 10^{23}, and 10^{24} Pa s, and set the plate boundary viscosity to 10^{19} or 10^{20} Pa s. These three viscosity profiles, three slab/lithosphere viscosities, and two plate boundary viscosities yielded 18 combinations. We additionally conducted eight simulations without dislocation creep in the upper mantle, such that viscosity depends only on temperature and pressure, with no strain rate dependence. These eight simulations are otherwise identical to eight of those described above, with parameters centered around those of our reference simulation. See Table 2 for a full listing of simulations and the rheological parameters for each.

Similarly, the thermal structure of the mantle is uncertain. In addition to varying the rheological parameters for a common thermal structure, we therefore performed five simulations using the reference rheological parameters but with different input thermal structures (Table 3). In addition to using SAVANI, we also used the TX2019slab whole-mantle shear velocity model for thermal structures below 300 km, which includes explicit representations of upper mantle slabs (Lu et al., 2019). For each, we also we performed a simulation replacing upper mantle velocity structure with the SL2013sv upper-mantle shear velocity model (Schaeffer & Lebedev, 2015). We also performed a simulation with lower-mantle tomography only, such that lateral heterogeneity in the upper mantle was only due to the lithosphere and slabs, as described above. To assess the influence of slabs beyond the extent of the Slab2 model, we additionally performed a simulation where we added a westward-extending slab "tail" to the Japan slab along the base of the upper mantle. The Japan slab tail is imaged clearly in tomographic imaging studies extending westwards along the mantle transition zone for a lateral distance of some 2,000 km (Fukao & Obayashi, 2013; Li et al., 2008), but is not included in the Slab2 Japan slab geometry. To construct this additional slab portion, we extended the Japan slab between 27° and 52° north westward from the westernmost limit of its geometry in Slab2, extending to the line between the points (109°E, 27°N) and (120°E, 52°N), after X. Liu et al. (2017).

3. Results

3.1. Model Validation

To validate the first-order behavior of our simulations, we first examine the degree to which our simulations reproduce plate velocities and the long wavelength geoid, which are well-constrained for the real earth. We show the surface velocity field from our reference model in Figure 2a, which we compare to the observed plate velocities for Earth (Bird, 2003) in the no-net-rotation reference frame (Figure 2b). Our models produce largely plate-like behavior of rigidly rotating plates, as a result of the strong lithosphere separated by weak zones at plate boundaries, with some non-platelike intraplate deformation. The plate motions in our model are primarily driven by slab pull at subduction zones, with movement of the subducting plate toward the trench, as well as basal traction from mantle flow (e.g., Becker & O'Connell, 2001; Conrad & Lithgow-Bertelloni, 2002; Lithgow-Bertelloni & Richards, 1998). As a result, the relative motions at plate boundaries reproduce those of Earth to first order, with convergence at subduction zones, divergence at mid-ocean ridges, and faster velocities for plates with attached slabs (Forsyth & Uyeda, 1975). Our model accurately captures the motions of the Pacific, Australian, and Cocos plates that subduct at one or more of their boundaries, as well as other plates such as North America, Eurasia, and Antarctica. However, our model fails to reproduce the rapid eastward motion of the Nazca plate or the direction of motion of the slow-moving African plate. The overall patterns and directions of surface velocity are consistent for models with and without non-linear dislocation creep (Becker, 2006), but the magnitudes vary

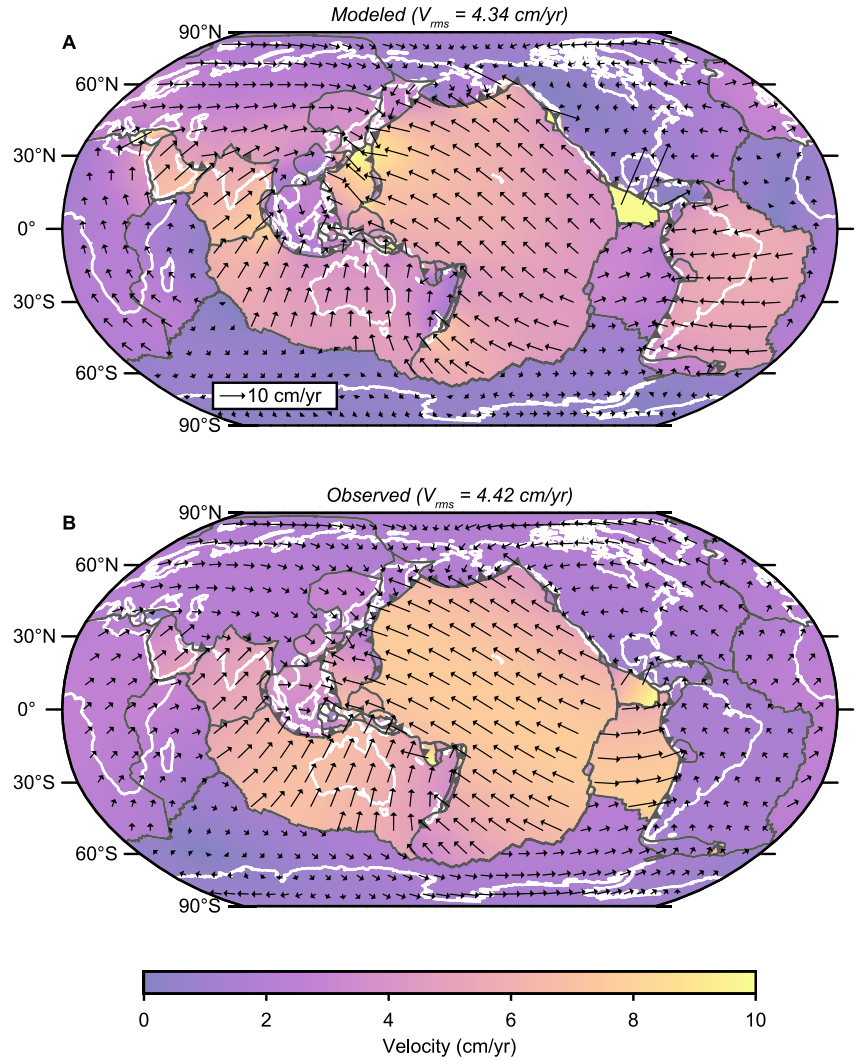

Figure 2. Surface plate velocities. (a) Surface velocity field from our reference simulation (see text for details). (b) Plate velocities from Bird (2003), converted to the no-net-rotation reference frame. Thin gray lines denote plate boundaries. Colors show velocity magnitude; arrows show both magnitude and direction (see legend). Both panels are plotted with the same velocity scale. Gray lines denote plate boundaries (Bird, 2003).

with rheologic parameters, in particular the background viscosity profile and the plate boundary viscosity, with higher values for each serving to reduce the surface velocities (e.g., Osei Tutu et al., 2018; Saxena et al., 2023; Stadler et al., 2010).

We can similarly compare the long-wavelength geoid anomaly (up to spherical harmonic degree and order 20) predicted from our reference model (S. Liu & King, 2019) to the observed geoid (Lemoine et al., 1998) (Figure S2 in Supporting Information S1). The predicted geoid anomaly reflects both density variations from the input thermal structure and dynamic topography from the resulting mantle flow (Hager, 1984; Hager et al., 1985). Our model reproduces the circum-Pacific geoid highs over major subduction zones, as has been replicated in numerous previous studies (e.g., Cadek & Fleitout, 2003; Hager & Richards, 1989; Steinberger, 2000), but somewhat overpredicts the amplitude. This correspondence suggests that our model captures important components of subduction zone dynamics, with the mass excess from dense slabs exerting a stronger effect than the mass deficit from dynamic subsidence (Hager, 1984). In contrast, our model does not predict the North Atlantic geoid high or the Indian Ocean geoid low, suggesting that our model lacks important features of mantle structure or flow in those regions. The Indian Ocean geoid low, for example, has been attributed to either high density slab material in the upper mantle, lower density plume material in the upper mantle, or some combination (Ghosh

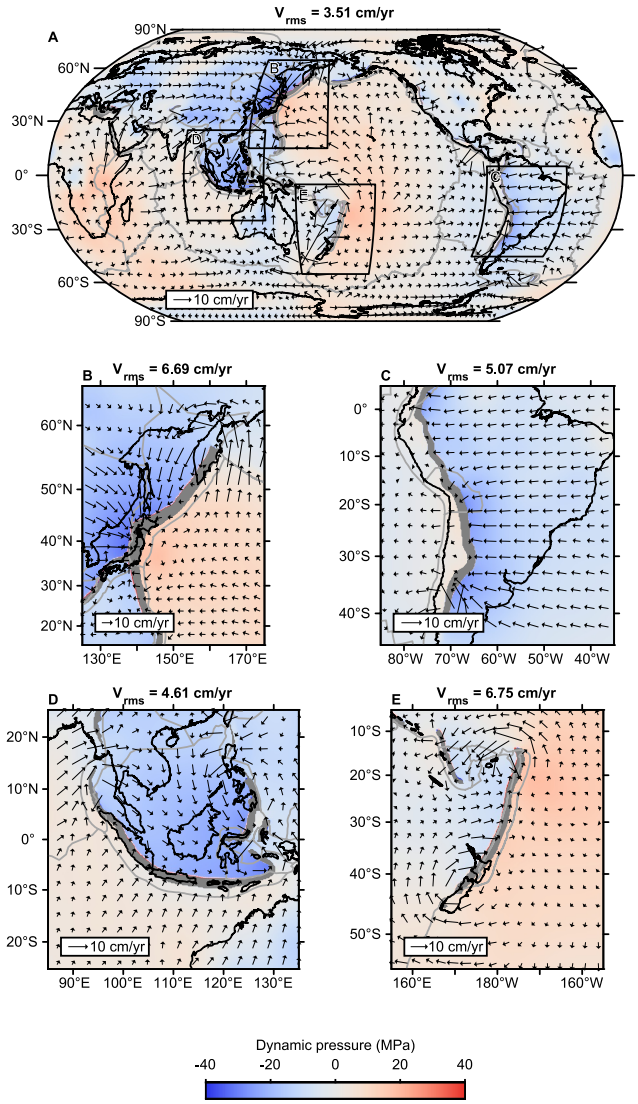

Figure 3. Dynamic pressure and horizontal velocity fields at 200 km depth from our reference simulation (see text for details). Locations of insets (b–e) are shown in (a) The length scaling for velocity vectors varies between panels to enhance clarity and is scaled to the region's root-mean-square velocity; see legend on each. Gray lines denote surface plate boundaries (Bird, 2003); dark gray regions outline the slab cross-section at 200 km depth.

et al., 2017; Spasojevic et al., 2010; Steinberger et al., 2021). Unlike the surface velocities, the amplitude of the geoid anomaly is relatively insensitive to our rheological parameters as it depends only on relative spatial changes in viscosity rather than absolute magnitude, such as the viscosity increase at 660 km (Hager et al., 1985). The first order agreement between our simulations and observations suggests that our models capture much of the important dynamics of upper mantle convection, particularly of slabs and their effects on plate velocities and geoid highs at convergent plate boundaries.

3.2. Sub-Surface Pressure and Flow at Subduction Zones

While the surface velocity field and geoid provide important model validation, our primary targets of interest are the pressure and flow within the mantle interior, for which we have no such direct measurements. In Figure 3, we show the dynamic (non-lithostatic) pressure and horizontal velocity field for our reference simulation at a depth of 200 km, both for the global domain and zoomed in around four major subduction zones. The lithostatic pressure is computed by integrating the density profile for the spherically averaged lithospheric thickness from the surface to 200 km depth. The dynamic pressure is the full pressure field less this quantity. Near subduction zones, we observe regions of high pressure underneath slabs and low pressure underneath the overriding plates. This across-slab pressure difference partially balances, and is therefore dictated by, the negative buoyancy of the dense slab (A. F. Holt & Royden, 2020; McKenzie, 1969; Stevenson & Turner, 1977; Tovish et al., 1978). The wedge-directed decrease in pressure, which has been explored in previous regional (Piromallo et al., 2006; Stegman et al., 2006) and global subduction modeling studies (A. F. Holt, 2022), decreases toward the slab edge; this across-slab difference and along-strike lateral gradient produce toroidal return flow around the slab edge from behind the slab toward the overriding plate (Dvorkin et al., 1993; Funiciello et al., 2004; Jadamec & Billen, 2010; Kincaid & Griffiths, 2003).

While the velocity and pressure fields shown in Figure 3 are for a single simulation only, we assess the mantle flow around subduction zones for the full suite of 18 simulations, each with the same input thermal structure but different rheological parameters (Runs 1–18, see Methods). For each simulation, we extract the velocity and pressure at different depths within the upper mantle by projecting down-dip from the trench to the specified depth. This approach fails at the eastern edge of the Sumatra trench where it curves back on itself, so we only consider this trench west of the recurve and omit the portion east of Timor Leste. At each specified depth, we extract the velocity and pressure at a horizontal distance of 200 km from both the upper and lower slab surfaces, which yields the near-slab flow and pressure within the mantle wedge and sub-slab regions, respectively. For the flow, we compare the horizontal azimuth to the local slab strike, allowing us to characterize the mantle flow near slabs in a consistent manner for different subduction zones. We then compute the circular mean and standard deviation (SD) of this quantity at each point across all simulations, which we use to show the robust flow features that emerge consistently from our ensemble (Figure 4). We chose 200 km to be sufficiently far from the slab to capture upper mantle flow but close enough to be within the influence of the subduction zone, thus showing the relationship and degree of coupling between slab motion and broader scale mantle flow. In Figure 4, we show this mean slab-relative flow azimuth at 200 and 400 km depth for 18 simulations, averaged along the strike for 500-km subduction zone segments. We similarly show the SD of the same quantity in Figure S3 of Supporting Information S1. For most segments, we find good agreement among our different simulations: 56% of the segments shown in Figure 4 have a SD less than 15° among the 18 simulations, 79% have a SD less than 30°, and 91% have a SD less than 45°.

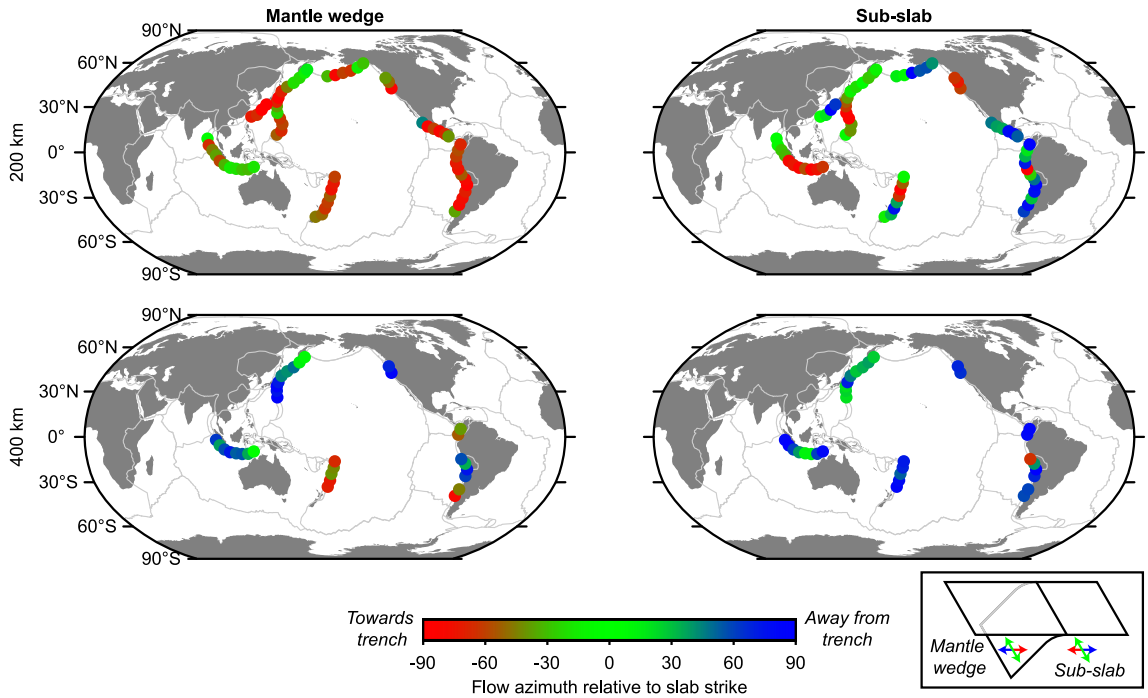

Figure 4. Segment-averaged flow azimuth relative to slab strike for 18 simulations (see text for details). For clarity, we only show the large circum-Pacific slabs discussed in the text. Velocity azimuth was extracted from the mantle wedge (left column) and sub-slab (right column) regions at 200 km (top row) and 400 km (bottom row) depths from the surface. Gray lines denote plate boundaries (Bird, 2003). The inset at the upper right shows a schematic subduction zone with flow directions colored as in the plots. The decreased number of points at 400 km depth reflects slabs that do not extend to 400 km depth in Slab2.

We observe several general patterns of mantle flow at subduction zones, particularly for the large circum-Pacific subduction zones, which are sketched in Figure 5. In general, the flow of the asthenospheric mantle is often coupled to the converging plates and slabs at shallow depths within the upper mantle, both above and below the slabs (i.e., in the mantle wedge and sub-slab regions). This pattern is apparent in Figures 3 and 4, which show a preponderance of convergent flow toward the trench from both sides of the slab at 200 km depth (Figure 5a). While these figures do not show the vertical component of flow, this component is typically downwards, following the slab. This pattern changes deeper within the upper mantle as the flow reverses away from the trench. This is apparent in Figure 4, in which the flow at 400 km depth largely mirrors that at 200 km, flowing away from the trench instead of toward. This is the manifestation of upper mantle convective cells localized by the 660 km boundary; the shallow convergent flow is balanced by deeper return flow away from the trench (Schubert & Turcotte, 1972; Schubert et al., 1978).

While this pattern of slab-coupled flow holds across much of the extent of many subduction zones, we observe a characteristic deviation toward the edges of slabs as the flow transitions from poloidal prismatic flow to toroidal flow around the edge of the slab (Figures 3, 4, 5b, and 5c). This flow typically transports material from the sub-slab region into the mantle wedge in response to downward motion of the negatively buoyant slab and slab roll-back toward the subducting plate. This flow is driven by the difference in dynamic pressure across the slab, with high pressure below and low pressure above. Sub-slab pressure is highest in the center of the slab and decays toward the edge, creating along-strike pressure gradients that drive the rotation of flow from slab-perpendicular to slab-parallel moving from the center to the edges of the slab in Figures 3 and 4 (Dvorkin et al., 1993; Funiciello et al., 2004). However, not all subduction zones conform fully to these general patterns of slab-coupled flow transitioning to around-slab toroidal flow at the edges; some subduction zones instead show more complex behavior or deviate from these trends, which we describe further in the Discussion (Figures 3 and 4).

3.3. Effects of Variable Model Inputs

The model runs with different density structures derived from tomography show largely similar upper mantle flow and pressure patterns, particularly near subduction zones, although there is some variation (Figures S4–S7 in

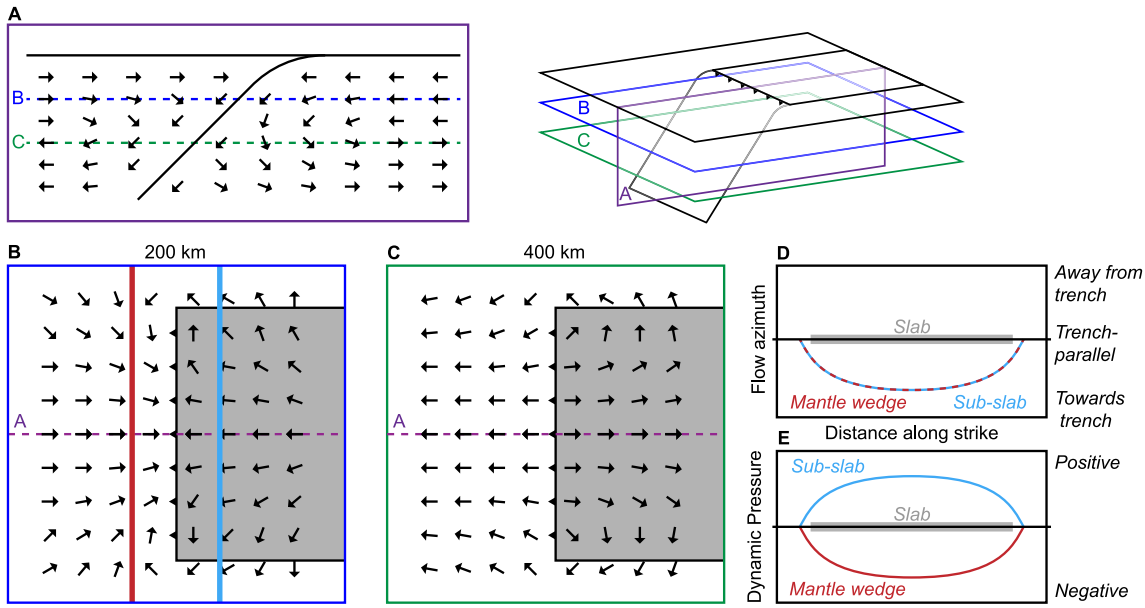

Figure 5. Idealized flow pattern around a schematic subduction zone. Panels (a–c) show the flow pattern at three cross-sections, as shown in the upper-right legend. Panel (a) is a vertical cross-section at the center of the slab showing poloidal flow; panels (b and c) are horizontal cross-sections at ~200 and ~400 km depth showing the planform flow geometry and transition to toroidal flow toward the slab edges (see legend at upper right for locations of cross-sections). Panels (d and e) show the flow azimuth and dynamic pressure extracted at 200 km depth within the near-slab asthenospheric mantle, as a function of distance along the strike from profiles on either side of the slab (see blue and red lines in panel (b) for locations of profiles). (d) Flow azimuth as a function of distance along the strike, showing similar patterns on both sides of the slab of rotation from slab-perpendicular toward-trench flow to toroidal slab-parallel flow toward the slab edge. (e) Dynamic pressure along the strike, showing the opposite effects of the negatively buoyant slab highest at the center, decaying toward the edges.

Supporting Information S1). Omitting upper mantle tomography reduces the across-slab pressure difference at subduction zones relative to all models that include any of the three choices of upper mantle tomography (Figure S5 in Supporting Information S1). The SL2013sv model reduces the pressure differences relative to TX2019slab or SAVANI, although predicts greater pressure differences than models with no upper mantle tomography. Generally, however, the predicted upper mantle flow shows similar patterns regardless of the choice of tomography model, especially near subduction zones.

We also vary the rheological parameters in models with a common input thermal structure. Changing each of the three viscosity parameters (ambient mantle viscosity, slab and plate strength, and plate boundary strength) affects the flow speed in the upper mantle, with an increase in each causing a decrease in flow speed. Increasing the average upper mantle viscosity at 330 km depth from 1×10^{21} Pa s to 2×10^{21} Pa s causes a ~2.5× average decrease in near-slab upper mantle velocity; the increase from 2×10^{21} to 3×10^{21} Pa s causes an additional ~2.7× decrease. Changing the slab viscosity from 10^{22} to 10^{23} Pa s decreases near-slab flow on average by a factor of 2.1; increasing from 10^{23} to 10^{24} decreases near-slab flow by a factor of 1.8 (Alisic et al., 2010; Wu et al., 2008). A ten-fold increase in the plate boundary viscosity, from 10^{19} to 10^{20} Pa s, causes a ~20% average decrease in near-slab flow velocity. However, these changes in flow speed do not have systematic effects on the orientation and spatial pattern of mantle flow near subduction zones, and primarily serve to scale the flow velocity magnitudes (Figures S8–S13 in Supporting Information S1). In contrast, the inclusion of dislocation creep affects both the magnitude and patterns of flow (Figures S14–S16 in Supporting Information S1). Relative to simulations without dislocation creep, the inclusion of dislocation creep reduces asthenospheric viscosity and increases upper mantle flow speeds preferentially in rapidly deforming regions such as subduction zones, increasing lateral viscosity and velocity gradients in these regions.

4. Discussion

Our model ensemble reveals many robust features of upper mantle flow and pressure across different simulations. Some of these regional flow regimes are similar among different subduction zones and exhibit the patterns summarized in the previous section, while other regions exhibit anomalous behavior. Some subduction

zones feature flow on one side consistent with global patterns but anomalous flow on the other side. We first discuss the mantle regions that display similar flow patterns, the consistent features among them, and their common characteristics that cause them to behave similarly. We then discuss the regions that deviate from the common pattern and potential reasons for their anomalous behavior. We also discuss the role of mantle rheology in patterns of mantle flow and compare the first order trends to seismological constraints on mantle anisotropy.

4.1. Conforming Subduction Zones

Regions that conform well in our simulations to the idealized subduction zone flow pattern sketched in Figure 5 include the mantle on both sides of the Kuril-Japan-Izu-Bonin-Mariana (IBM) trenches, the mantle underneath the Sumatra slab, the mantle wedge over the Ryukyu slab, and the mantle wedge over the South American (Nazca) slab. Each of these displays the characteristic pattern of toward-trench flow at 200 km depth, away-from-trench flow at 400 km depth, and the rotation from slab-perpendicular to slab-parallel flow toward the edges of the slabs to accommodate flow around the slab edge toward the overriding plate. These subduction zones have several attributes in common. Except for Ryukyu, each of these subduction zones is greater than 5,000 km in along-strike length, and the top surface of the slab extends to at least 500 km depth within the mantle. Moreover, the Kuril-Japan-IBM, Ryukyu, and Sumatra slabs are all at least 100 km thick. These characteristics mean that these large and extensive negatively buoyant slabs induce relatively large dynamic pressure signals (as this pressure balances the large density anomalies), and thus dominate and drive the mantle flow around them. As a result, the emergent flow is similar to that found using idealized subduction models that feature only a single slab with no other mantle structure—either in Cartesian domains (Funiciello et al., 2004; Funiciello, Faccenna, et al., 2003; Piromallo et al., 2006) or, more recently, in global domains (Chen et al., 2022; A. F. Holt, 2022). A similar around-slab toroidal flow regime was observed at 400 km depth within Alisic et al.'s (2012) geographically tailored models that are broadly similar to those presented here. However, toward the center of their slabs, flow is directed toward the trench in the mantle wedge in all the cases shown. This flow pattern suggests a stronger role for slab rollback and increased negative pressure in the mantle wedge, in contrast to our observations of return flow away from the trench at that depth on both sides of the slab. They do not show shallower flow fields to compare to our results at 200 km depth.

The pattern of along-strike variability in flow and rotation from slab-perpendicular to slab-parallel flow azimuth is directly related to spatial gradients in dynamic pressure, and in particular the positive pressure buildup behind and beneath the slab (Figure 6). A linear slab of infinite lateral extent would have uniform along-strike positive pressure beneath the slab, set by the negative buoyancy and confining effect of the slab, and would hence drive no slab parallel flow. However, slabs and subduction zones on Earth are finite, and the pressure build-up behind the slab must decay toward the unconfined edges. The resulting along-strike pressure gradient therefore drives toroidal flow around the slab edge from the sub-slab mantle into the mantle wedge (Jadamec & Billen, 2010; Piromallo et al., 2006; Royden & Husson, 2006; Schellart et al., 2007); such toroidal flow patterns have also been inferred from shear wave splitting measurements of upper mantle seismic anisotropy (Civello & Margheriti, 2004; Walpole et al., 2017). For the Kuril-Japan-IBM subduction zone (blue curves), we observed enhanced along-strike pressure gradients toward the edge of the slabs, corresponding to regions of slab-parallel flow. We note that the abrupt jump in mantle wedge pressure near the center of the Japan slab is due to the junction with the Ryukyu slab and the relative confinement of mantle wedge material on either side of the slab. Aside from this local complexity, Kuril-Japan-IBM exhibits the flow and pressure characteristics common to other large subduction zones and is sketched in Figure 5.

4.2. Anomalous Subduction Zones

In contrast, some regions, such as the Sumatra mantle wedge or the Ryukyu sub-region, deviate from this idealized behavior due to interactions with other nearby subduction zones or global-scale upper mantle flow (Figure 7). In the case of Sumatra, the mantle above the slab is dragged eastward by the subduction zones to the east (Figure 3d), which drives largely eastward slab-parallel flow in the mantle wedge (Figure 4). Beneath the Ryukyu slab, flow is dominated by the Izu-Bonin subduction zone to the east, causing eastward flow away from the trench and a negative sub-slab pressure signal due to the interference of the Japan-IBM slab (A. F. Holt et al., 2018) (Figure 3b). These examples demonstrate that the relatively local flow around subduction zones can also be controlled by longer-wavelength flow patterns, and that large subduction zones have effects on flow that

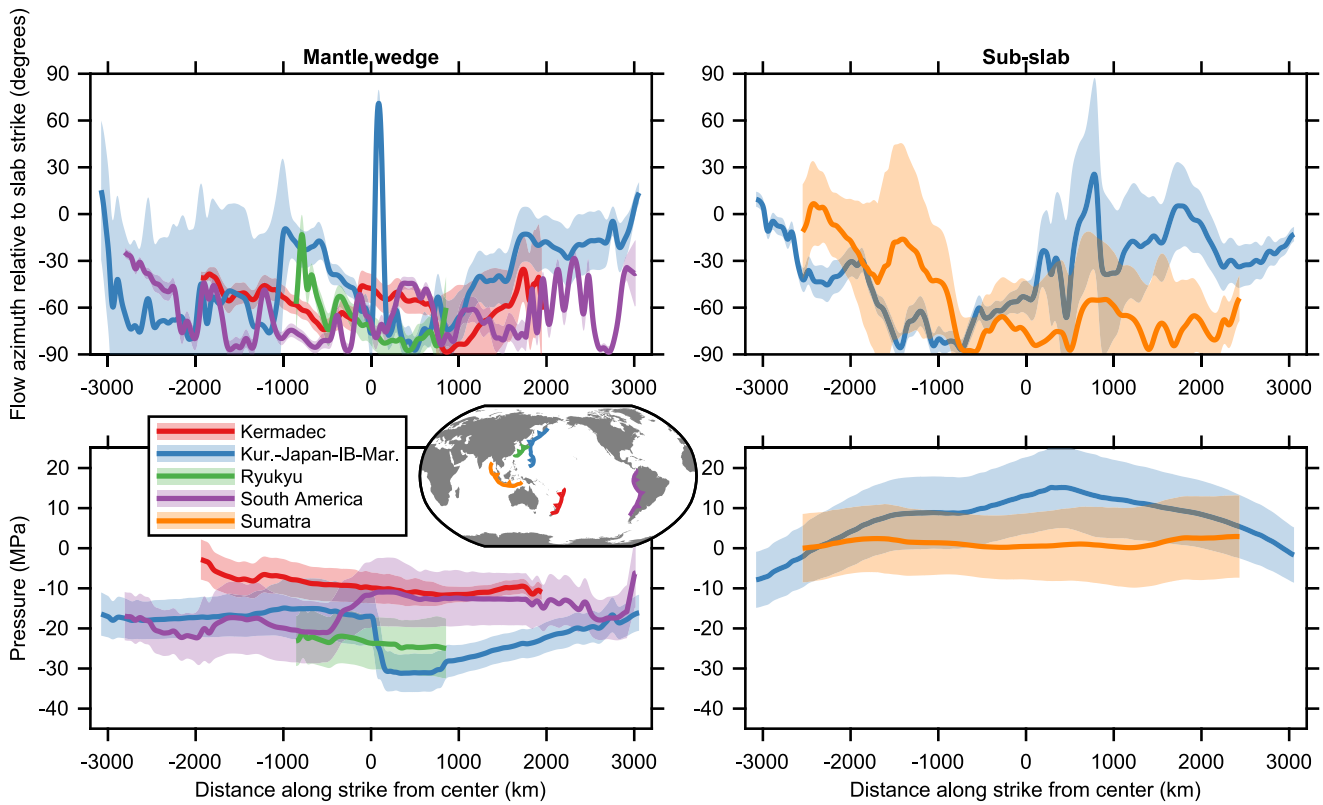

Figure 6. Along-strike profiles of flow azimuth and dynamic pressure for conforming subduction zones at 200 km depth. Profiles were extracted 200 km horizontally from upper and lower slab surfaces as described in the text. Solid lines denote the average of 18 model runs as described in the text; shaded regions denote ±1 SD. Profiles are smoothed with a Gaussian filter (σ = 25 km). Kur., Kurile; IB, Izu-Bonin; Mar., Mariana.

extend to other regions beyond their immediate surroundings. This confirms previous assertions (Hager & O'Connell, 1978; A. F. Holt & Royden, 2020; Husson, 2012) by quantifying these linkages within multi-scale models that directly capture both regional and global-scale flow fields. Mantle flow thus forms a powerful linkage between different subduction zones, as has been shown in past regional models containing either two separate slabs or two slabs connected via an intervening plate in a double subduction system (e.g., A. F. Holt et al., 2017; Király et al., 2016), with smaller subduction zones especially sensitive to regional patterns of mantle flow beyond those generated locally. Our models show potential linkages across length scales longer than the 660-km thickness of the upper mantle convection cell that has been argued in past studies (Király et al., 2016, 2017; Peral et al., 2018), potentially due to subduction-induced mantle flow cells that traverse beyond the upper-to-lower mantle viscosity jump (e.g., Faccenna et al., 2013, 2017; Husson, Conrad, & Faccenna, 2012; Husson, Guillaume, et al., 2012).

Furthermore, these examples illustrate that slabs form effective barriers to flow (Royden & Holt, 2020; Royden & Husson, 2006), isolating pressure and flow on one side from the other. For the same slab motion, the mantle flow can be close to ideal on one side of the slab but deviate substantially on the other side due to different influences on the asthenospheric flow on the sub-slab and mantle wedge sides. For example, the sub-slab mantle of the Sumatra subduction zone exhibits conforming behavior, since there are no other subduction zones or other major features of upper mantle flow to the southwest that overpower the influence of the subducting slab. However, the Sumatra mantle wedge exhibits largely eastward slab-parallel flow due to the competing influence of other subduction zones to the east and the resulting along-strike pressure gradient. The presence of the slab prevents this influence from affecting the sub-slab mantle as well. The motion of the Sumatra slab, which is the same for both sides, is thus able to dominate flow in the sub-slab region but not in the mantle wedge. The Ryukyu slab exhibits a similar but reversed pattern, with the mantle wedge exhibiting near-ideal behavior, isolated from the contaminating influence of the Izu-Bonin-Mariana subduction zone that dominates the Ryukyu sub-slab mantle.

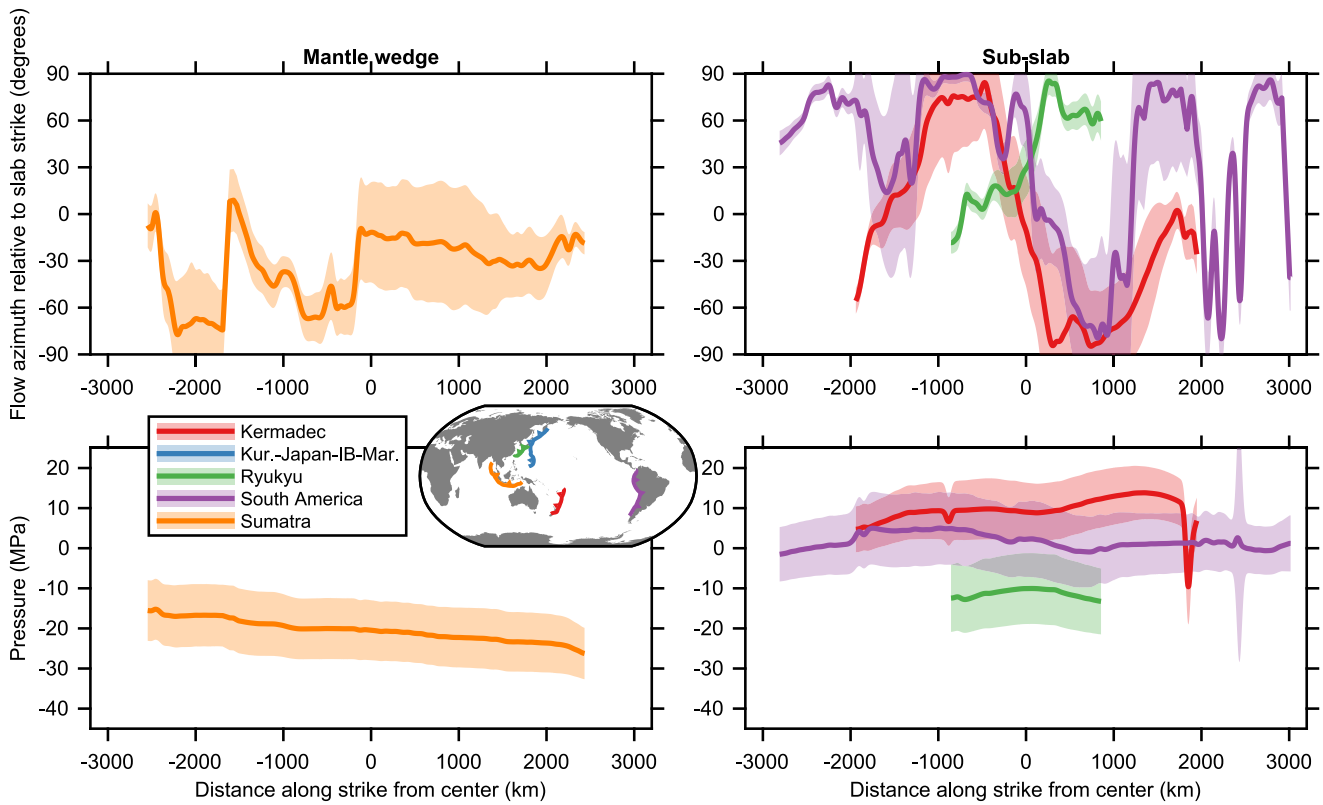

Figure 7. Along-strike profiles of flow azimuth and dynamic pressure for anomalous subduction zones at 200 km depth. Profiles were extracted 200 km horizontally from upper and lower slab surfaces as described in the text. Solid lines denote the average of 18 model runs as described in the text; shaded regions denote ±1 SD. Profiles are smoothed with a Gaussian filter (σ = 25 km). Kur., Kurile; IB, Izu-Bonin; Mar., Mariana.

In areas with very low velocity magnitudes, small vector changes in velocity can create large changes in the azimuth. Regions in this category include the sub-slab mantle under the Kermadec and South American (Nazca) slabs, which exhibit noisy flow azimuth values with no clear trend (Figures 3 and 4). Due to the low magnitudes, flow directions in these regions can be sensitive to the chosen reference frame. We use the no-net-rotation reference frame to facilitate direct comparison to observed plate velocities, but rotating into a different choice of reference frame changes the velocity magnitudes in these regions and potentially the azimuth as well, and thus affects the interpreted flow patterns. For example, a shift into the hotspot reference frame adds a large westward rotation (Euler pole at 56°S, 70°E) with a maximum magnitude of ∼5 cm/yr (Gripp & Gordon, 2002). This rotation is larger than and in the opposite direction of the mantle flow beneath the Kermadec slab, meaning that in the hotspot reference frame (Figure S17 in Supporting Information S1), the Kermadec sub-slab region reverses and flows toward the trench, which conforms to the idealized flow pattern described earlier (Figure 5). However, the rotation into the hotspot reference frame is in the same direction as the Nazca sub-slab mantle flow, meaning that this region still flows away from the trench in the hotspot reference frame, with a larger magnitude than in the no-net-rotation frame (Figure S4 in Supporting Information S1). An alternative explanation is therefore required to explain the anomalous flow in that region, potentially related to the high along-strike variability in slab shape and flat-slab subduction.

4.3. Influence of Slab Geometry on Flow and Pressure Patterns

The pressure around subduction zones is largely driven by the negative buoyancy of the dense slab, which is a function of the slab thickness and dip (A. F. Holt & Royden, 2020; McKenzie, 1969; Stevenson & Turner, 1977; Tovish et al., 1978). In our models, we find that the across-slab pressure difference at 200 km depth is strongly and significantly correlated with the slab buoyancy computed from Slab2 as used in our input thermal structure (R^2 = 0.84, p < 0.0001; Figure S18 in Supporting Information S1). However, we note that the absolute pressure difference is systematically reduced relative to buoyancy (Figure S18 in Supporting Information S1), indicating

that some of the buoyancy is supported by stresses within the slab rather than by external pressure. Although we use modern observed slab geometry as inputs for our instantaneous models, the evolution of slab dip through time depends in turn on mantle pressure and flow patterns. However, the across-slab pressure difference, which exerts a fundamental effect on subduction zone pressure and flow fields, should evolve quasi-statically with changing slab dips, subject to changes in intra-slab stresses from bending or other deformations.

In addition to factors such as slab extent and thickness, the planform geometry of the subduction zone plays an important role in determining the pressure build-up beneath the subducting slab. The Japan slab features an arcuate geometry with the concavity toward the subducting Pacific Plate, which traps material and inhibits lateral flow, enhancing the positive pressure build-up behind the concave slab (Figure 2b), and potentially causing the shallow slab dip (A. F. Holt & Royden, 2020). In contrast, the Sumatra subduction zone is convex toward the subducting plate (Figure 2d), and experiences substantially lower sub-slab pressure as a result (Figure 6). At a larger scale, dynamic pressure is ∼10 MPa greater beneath the Western Pacific than that beneath the Eastern Pacific. This Pacific Plate dichotomy, as argued by prior researchers (Husson et al., 2008), is due to the combined effects of rapid Pacific Plate motion and the lateral containment of the Western Pacific sub-slab mantle by old and relatively continuous slabs (e.g., A. F. Holt, 2022; A. F. Holt & Royden, 2020; Husson, Conrad, & Faccenna, 2012; Husson, Guillaume, et al., 2012).

Our instantaneous simulations use the present geometry as an input, but the development of curvature over time is itself a function of the dynamic pressure and resulting flow. In particular, the pressure pattern at large subduction zones such as Japan likely drive the curvature of the subducting slab by retarding trench retreat toward the center of the slab with the highest sub-slab pressure (e.g., Schellart et al., 2007). South America, although also curved and wide, shows a more complex signal in our models without a clear sub-slab pressure build-up toward the center, as has been argued elsewhere (Russo & Silver, 1994; Schellart et al., 2007; Schepers et al., 2017). This lack of sub-slab South American pressure build-up is likely due to a combination of the younger subducting plate age and thinner slab—which requires a lower across-slab pressure difference—and the relative dominance of negative pressure in the wedge beneath South America (Figure 3c) due to flow that is confined beneath a thick overriding plate (Manea et al., 2012; O'Driscoll et al., 2012). We also note that our modeled surface plate velocities of the Nazca and South American plates differ from those observed (Figure 2); although we find similarly fast convergence, our models predict that most of this convergence is accommodated by westward motion of the South American plate rather than by eastward motion of the Nazca plate. This mismatch may affect the pressure and velocity fields near the slab.

4.4. Effects of Variable Model Inputs

4.4.1. Mantle Structure

The reduction in the across-slab pressure difference when upper mantle tomography is omitted indicates that the near-slab density anomalies from tomographic models are of the same sign as the dense slabs we model from Slab2, increasing the negative buoyancy of these features in our modeled mantle. This is likely due to the "smearing" of slabs in tomography models, in which the dense anomalies are lower in amplitude but larger in extent than the discrete slabs we model from Slab2, such that their inclusion creates additional negative buoyancy outside our modeled slabs. The relatively modest effect on flow patterns from the addition of upper mantle thermal structure derived from tomographic models indicates that upper mantle pressure and flow, especially near subduction zones, are dominated by slabs and their density anomalies, rather than by longer-wavelength but lower-amplitude features. Including tomography-derived thermal anomalies affects pressure and flow most strongly in plate interiors far from subduction zones, where there is no thermal heterogeneity from slabs and the lithosphere. However, our approach may fail to incorporate some aspects of the Earth's deeper structure, including high-resolution features that are not well captured by tomography or inaccuracies in our conversion from wave speed to temperature.

The Slab2 data set that we used to reconstruct the extent of subducted slabs within Earth's mantle is a conservative estimate of slab length with slabs confined to the upper mantle. Some slabs, such as Japan, extend further along the 660-km mantle transition zone, while others, such as the Mariana slab and Peru portion of the Nazca slab, extend into the lower mantle (Fukao & Obayashi, 2013; Li et al., 2008; van der Hilst et al., 1997). Our simulation incorporating an additional westward-extending "tail" of the Japan slab shows modestly different results from our reference case, indicating that these additional features can affect upper mantle flow and pressure (Figure S19 in Supporting Information S1). In particular, we observed a reduction in the Pacific Plate speed and increased

negative pressure in the mantle wedge. However, the general patterns of upper-mantle flow around the subduction zone are not substantially changed by the addition of the slab "tail," suggesting that, in our models and in this region, the slab extents from Slab2 include most of the thermal heterogeneity driving upper mantle flow. Moreover, the tomography models we use for lower-mantle structure do image some lower mantle slabs, which have been proposed to strongly affect the mantle flow regime (Faccenna et al., 2013; Husson, Conrad, & Faccenna, 2012; Husson, Guillaume, et al., 2012), although at a lower resolution and with lower amplitude than our upper mantle slabs reconstructed using Slab2. Our flow patterns therefore incorporate some of the flow effects associated with slabs that have penetrated into the lower mantle but at a reduced magnitude relative to regional subduction models that include coherent, penetrating lower mantle slabs (e.g., Dal Zilio et al., 2018; Faccenna et al., 2017).

4.4.2. Mantle Rheology

Three of the parameters we vary, the average (reference) upper mantle viscosity (Figures S8 and S9 in Supporting Information S1), the slab and lithosphere strength (Figures S10 and S11 in Supporting Information S1), and the plate boundary strength (Figures S12 and S13 in Supporting Information S1), primarily serve to scale the magnitude of flow without changing the underlying patterns or relative spatial variation. Increasing the viscosity of any of the three components, which increases the viscous resistance to buoyant stresses, naturally reduces the average mantle flow velocity for the same thermal structure (e.g., Becker, 2006; Osei Tutu et al., 2018). Increasing the slab and plate interface viscosity elevates plate resisting forces associated with slab bending and plate interface shear, respectively, and hence also reduces plate speeds (Behr & Becker, 2018; Buffett, 2006; Conrad & Hager, 1999; Saxena et al., 2023; Wu et al., 2008). A reduction in surface plate speed in turn reduces three-dimensional flow velocities throughout the upper mantle.

In contrast to these parameters, the non-linear dislocation creep affects the spatial pattern of upper-mantle flow as well as its overall magnitude. The detection of upper-mantle seismic anisotropy, likely induced by the lattice-preferred orientation of olivine crystals (Nicolas & Christensen, 1987), signifies the widespread operation of dislocation creep in the upper mantle, with this deformation mechanism dominating in most of the upper mantle to a depth of at least 400 km (Behn et al., 2009). This effect introduces strain rate-dependent viscosity and hence decreases mantle viscosity in rapidly deforming regions (Becker, 2006; Christensen, 1984; Čadek et al., 1993). In addition to decreasing the effective viscosity for most of the upper mantle in our models, and thus increasing the average flow velocity, this strain rate-dependent deformation localizes and enhances flow in rapidly shearing regions, such as adjacent to slabs or in the asthenosphere immediately beneath lithospheric plates. In our models incorporating dislocation creep, this process accommodates a substantial portion of upper-mantle strain, particularly in rapidly deforming regions around subduction zones, where it typically accommodates >75% of total strain (Figure S20 in Supporting Information S1). This near-slab and sub-plate weakening effect of dislocation creep has also been demonstrated in previous regional analytical subduction zone models (Tovish et al., 1978) and time-dependent subduction models (e.g., Billen & Hirth, 2005, 2007; A. F. Holt & Becker, 2017), and convection models (Becker, 2006; Christensen, 1984; Semple & Lenardic, 2021; Čadek et al., 1993). As a result of this localized weakening, our simulations with and without dislocation creep produce substantially different patterns of subduction zone flow (Figures 3 and 8; Figures S14–S16 in Supporting Information S1); the addition of dislocation creep increases lateral variation in viscosity and velocity (Figure 3 and Figure S14 in Supporting Information S1). This effect localizes and enhances around-slab toroidal flow decoupled from surface plate motions, consistent with previous regional modeling (Billen & Jadamec, 2012; Jadamec & Billen, 2010, 2012).

The low-viscosity zones produced by dislocation creep adjacent to slabs decrease the coupling between slabs and the asthenosphere, which is evident from the near-slab flow field (Figure 8). Without dislocation creep, we observe stronger coupling, shown by a near-universal trend of toward-trench flow at shallow depths in the sub-slab mantle and away-from-trench flow at deeper depths in the mantle wedge (Figure 8 and Figure S15 in Supporting Information S1). Both trends reflect the horizontal component of mantle flow highly coupled to the subducting slab, whereas the addition of dislocation creep decreases this coupling and facilitates more complex flow patterns (Figure 4). The decrease in slab-perpendicular coupled flow from the addition of dislocation creep causes some subduction zones, such as the Kermadec Trench, to deviate from idealized behavior even though they conform when the dislocation creep is not included (Figure 8). Shear wave splitting measurements of seismic anisotropy suggest a mix of slab-parallel and slab-perpendicular sub-slab flow globally (Walpole et al., 2017), as in our simulations with dislocation creep, although other previous studies have suggested largely slab-parallel

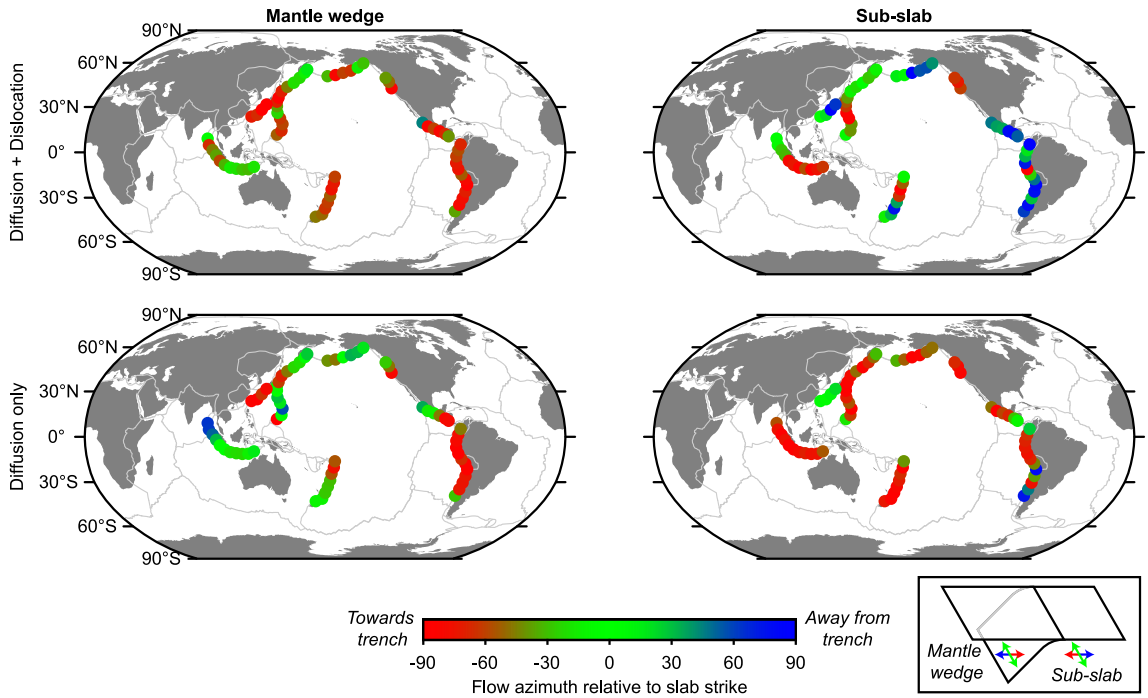

Figure 8. Comparison of near-slab flow azimuth with and without dislocation creep at 200 km depth. The upper row shows results from 18 simulations with dislocation creep (same as Figure 4). Lower row shows the analogous result for eight simulations without dislocation creep (same as Figure S15 in Supporting Information S1).

flow beneath slabs at subduction zones (Long, 2013; Long & Silver, 2008; Lynner & Long, 2014). In contrast, our simulations without dislocation creep show enhanced slab-mantle coupling and hence largely slab-perpendicular flow, which conflicts with the seismic evidence. Our models therefore suggest that dislocation creep is a key process necessary to reproduce the nearly uniform distribution of azimuths found in seismic anisotropy (Walpole et al., 2017). Additionally, the influence of longer-wavelength mantle convection on mantle flow has also been argued to increase the proportion of slab-parallel flow relative to the idealized subduction model (Paczkowski, Montési, et al., 2014; Paczkowski, Thissen, et al., 2014). Although we do not explicitly test this hypothesis, our models combining regional and longer-wavelength mantle structures produce a mixture of slab-parallel and slab-perpendicular flow.

In addition to its effect on the coupling between upper mantle flow and slab motion, dislocation creep also affects along-strike patterns of pressure and flow in front of and behind slabs. By increasing the relative spatial variation in velocity and enhancing around-slab toroidal flow, this effect decreases the pressure difference across slabs (Figures 3, 6, and 7; Figures S14 and S16 in Supporting Information S1), since the pressure can be more easily relieved by the flow of material from beneath to above the slab. This decreased pressure difference, resulting from power law flow, has also been shown to increase slab dips in 2-D models (Billen & Hirth, 2005), although our models use observed slab dips as a fixed input. Furthermore, the lateral decay of pressure buildup extends over a wider region at the edges of the slabs with dislocation creep, with a reduced lateral pressure gradient (Figure 6 and Figure S16 in Supporting Information S1).

Our model comparisons confirm that dislocation creep exerts a strong influence on the effects of slabs on mantle flow by enhancing lateral variations in viscosity and velocity, increasing around-slab toroidal flow, and decreasing the pressure difference across slabs. By partially decoupling slab motion from upper mantle flow, dislocation creep also facilitates complex near-slab flow patterns that deviate from the idealized flow patterns exhibited by idealized subduction models but more closely agree with observational constraints.

5. Conclusions

We have embedded high-resolution models of Earth's lithosphere and slabs within global mantle flow models that include composite diffusion-dislocation creep rheology for Earth's mantle. The model outputs are physically

plausible Earth-like flow fields for mantle convection that permit the examination of the interactions between subduction and global mantle flow at regional and global scales. Dynamic pressure generated by negatively buoyant slabs is a primary driver of upper mantle flow. Subduction zones with thick and extensive slabs, such as Kuril-Japan-Izu-Bonin-Mariana, produce similar and relatively simple flow and pressure patterns; this is due to the dominant effect of these large local density anomalies relative to far-field effects. The downward motion of these slabs drives convergent flow in the shallow asthenosphere balanced by divergent return flow deeper in the upper mantle, with around-slab toroidal flow toward the slab edges. However, other subduction zones, such as Sumatra, do not conform to this canonical view of subduction-induced flow and are instead influenced by larger-scale mantle flow, including from flow driven by other subduction zones; this anomalous flow is enhanced by non-linear dislocation creep, which partially decouples upper mantle flow from slab motion. These findings illustrate the complex interactions between subduction zones and global mantle flow, and how subduction zone characteristics determine whether upper mantle flow is dominated by local subduction processes or longer-wavelength flow.

Data Availability Statement

All model inputs and ASPECT parameter files are available in a Zenodo repository (Goldberg & Holt, 2023).

Acknowledgments

SLG was funded by an NSF Earth Science Postdoctoral Fellowship award EAR-2204308 and AFH was partially supported by NSF EAR-2147997. Computational resources were provided by NSF ACCESS under allocation EAR180026 to AFH. This work has benefited from scientific discussions with Leigh H. Royden, Gregor P. Eberli, and Thorsten W. Becker. We also thank Nestor Cerpa, an anonymous reviewer, and the Associate Editor for helpful feedback on earlier versions of the manuscript. We thank the Computational Infrastructure for Geodynamics (geodynamics.org), which is funded by the National Science Foundation under award EAR-0949446 and EAR-1550901 for supporting the development of ASPECT.

References

Alisic, L., Gurnis, M., Stadler, G., Burstedde, C., & Ghattas, O. (2012). Multi-scale dynamics and rheology of mantle flow with plates. *Journal of Geophysical Research*, *117*(10), B10402. https://doi.org/10.1029/2012JB009234

Alisic, L., Gurnis, M., Stadler, G., Burstedde, C., Wilcox, L. C., & Ghattas, O. (2010). Slab stress and strain rate as constraints on global mantle flow. *Geophysical Research Letters*, *37*(22), L22308. https://doi.org/10.1029/2010GL045312

Auer, L., Boschi, L., Becker, T. W., Nissen-Meyer, T., & Giardini, D. (2014). *Savani*: A variable resolution whole-mantle model of anisotropic shear velocity variations based on multiple data sets. *Journal of Geophysical Research: Solid Earth*, *119*(4), 3006–3034. https://doi.org/10.1002/2013JB010773

Bangerth, W., Dannberg, J., Fraters, M., Gassmoeller, R., Glerum, A., Heister, T., & Naliboff, J. (2021a). ASPECT: Advanced Solver for Problems in Earth's ConvecTion, User Manual. https://doi.org/10.6084/M9.FIGSHARE.4865333

Bangerth, W., Dannberg, J., Fraters, M., Gassmoeller, R., Glerum, A., Heister, T., & Naliboff, J. (2021b). ASPECT v2.3.0. https://doi.org/10.5281/ZENODO.5131909

Becker, T. W. (2006). On the effect of temperature and strain-rate dependent viscosity on global mantle flow, net rotation, and plate-driving forces. *Geophysical Journal International*, *167*(2), 943–957. https://doi.org/10.1111/j.1365-246x.2006.03172.x

Becker, T. W., & Faccenna, C. (2009). A review of the role of subduction dynamics for regional and global plate motions. *Subduction Zone Geodynamics* (pp. 3–34). https://doi.org/10.1007/978-3-540-87974-9_1

Becker, T. W., & Faccenna, C. (2011). Mantle conveyor beneath the Tethyan collisional belt. *Earth and Planetary Science Letters*, *310*(3–4), 453–461. https://doi.org/10.1016/j.epsl.2011.08.021

Becker, T. W., & O'Connell, R. J. (2001). Predicting plate velocities with mantle circulation models. *Geochemistry, Geophysics, Geosystems*, *2*(12), 1060. https://doi.org/10.1029/2001gc000171

Behn, M. D., Hirth, G., & Elsenbeck, II, J. R. (2009). Implications of grain size evolution on the seismic structure of the oceanic upper mantle. *Earth and Planetary Science Letters*, *282*(1–4), 178–189. https://doi.org/10.1016/j.epsl.2009.03.014

Behr, W. M., & Becker, T. W. (2018). Sediment control on subduction plate speeds. *Earth and Planetary Science Letters*, *502*, 166–173. https://doi.org/10.1016/j.epsl.2018.08.057

Billen, M. I., & Gurnis, M. (2003). Comparison of dynamic flow models for the Central Aleutian and Tonga-Kermadec subduction zones. *Geochemistry, Geophysics, Geosystems*, *4*(4), 1035. https://doi.org/10.1029/2001GC000295

Billen, M. I., & Gurnis, M. (2005). Constraints on subducting plate strength within the Kermadec trench. *Journal of Geophysical Research*, *110*(B5), B05407. https://doi.org/10.1029/2004JB003308

Billen, M. I., & Hirth, G. (2005). Newtonian versus non-Newtonian upper mantle viscosity: Implications for subduction initiation. *Geophysical Research Letters*, *32*(19), L19304. https://doi.org/10.1029/2005gl023457

Billen, M. I., & Hirth, G. (2007). Rheologic controls on slab dynamics. *Geochemistry, Geophysics, Geosystems*, *8*(8), Q08012. https://doi.org/10.1029/2007gc001597

Billen, M. I., & Jadamec, M. (2012). Origin of localized fast mantle flow velocity in numerical models of subduction. *Geochemistry, Geophysics, Geosystems*, *13*(1), Q01016. https://doi.org/10.1029/2011gc003856

Bird, P. (2003). An updated digital model of plate boundaries. *Geochemistry, Geophysics, Geosystems*, *4*(3), 1027. https://doi.org/10.1029/2001GC000252

Buffett, B. A. (2006). Plate force due to bending at subduction zones. *Journal of Geophysical Research*, *111*(B9), B09405. https://doi.org/10.1029/2006JB004295

Cadek, O., & Fleitout, L. (2003). Effect of lateral viscosity variations in the top 300 km on the geoid and dynamic topography. *Geophysical Journal International*, *152*(3), 566–580. https://doi.org/10.1046/j.1365-246X.2003.01859.x

Čadek, O., Ricard, Y., Martinec, Z., & Matyska, C. (1993). Comparison between Newtonian and non-Newtonian flow driven by internal loads. *Geophysical Journal International*, *112*(1), 103–114. https://doi.org/10.1111/j.1365-246x.1993.tb01440.x

Chen, F., Davies, D. R., Goes, S., Suchoy, L., & Kramer, S. C. (2022). How slab age and width combine to dictate the dynamics and evolution of subduction systems: A 3-D spherical study. *Geochemistry, Geophysics, Geosystems*, *23*(11), e2022GC010597. https://doi.org/10.1029/2022gc010597

Chertova, M. V., Spakman, W., & Steinberger, B. (2018). Mantle flow influence on subduction evolution. *Earth and Planetary Science Letters*, *489*, 258–266. https://doi.org/10.1016/j.epsl.2018.02.038

Christensen, U. (1984). Convection with pressure-and temperature-dependent non-Newtonian rheology. *Geophysical Journal International*, *77*(2), 343–384. https://doi.org/10.1111/j.1365-246x.1984.tb01939.x
Civello, S., & Margheriti, L. (2004). Toroidal mantle flow around the Calabrian slab (Italy) from SKS splitting. *Geophysical Research Letters*, *31*(10), L10601. https://doi.org/10.1029/2004gl019607
Čížková, H., van Hunen, J., van den Berg, A. P., & Vlaar, N. J. (2002). The influence of rheological weakening and yield stress on the interaction of slabs with the 670 km discontinuity. *Earth and Planetary Science Letters*, *199*(3–4), 447–457. https://doi.org/10.1016/S0012-821X(02)00586-1
Conrad, C. P., & Hager, B. H. (1999). Effects of plate bending and fault strength at subduction zones on plate dynamics. *Journal of Geophysical Research*, *104*(B8), 17551–17571. https://doi.org/10.1029/1999jb900149
Conrad, C. P., & Lithgow-Bertelloni, C. (2002). How mantle slabs drive plate tectonics. *Science*, *298*(5591), 207–209. https://doi.org/10.1126/science.1074161
Dal Zilio, L., Faccenda, M., & Capitanio, F. (2018). The role of deep subduction in supercontinent breakup. *Tectonophysics*, *746*, 312–324. https://doi.org/10.1016/j.tecto.2017.03.006
Davies, D. R., Valentine, A. P., Kramer, S. C., Rawlinson, N., Hoggard, M. J., Eakin, C. M., & Wilson, C. R. (2019). Earth's multi-scale topographic response to global mantle flow. *Nature Geoscience*, *12*(10), 845–850. https://doi.org/10.1038/s41561-019-0441-4
Dvorkin, J., Nur, A., Mavko, G., & Ben-Avraham, Z. (1993). Narrow subducting slabs and the origin of backarc basins. *Tectonophysics*, *227*(1–4), 63–79. https://doi.org/10.1016/0040-1951(93)90087-z
Faccenna, C., Becker, T. W., Conrad, C. P., & Husson, L. (2013). Mountain building and mantle dynamics. *Tectonics*, *32*(1), 80–93. https://doi.org/10.1002/tect.20012
Faccenna, C., Oncken, O., Holt, A. F., & Becker, T. W. (2017). Initiation of the Andean orogeny by lower mantle subduction. *Earth and Planetary Science Letters*, *463*, 189–201. https://doi.org/10.1016/j.epsl.2017.01.041
Ficini, E., Dal Zilio, L., Doglioni, C., & Gerya, T. V. (2017). Horizontal mantle flow controls subduction dynamics. *Scientific Reports*, *7*(1), 7550. https://doi.org/10.1038/s41598-017-06551-y
Forsyth, D., & Uyeda, S. (1975). On the relative importance of the driving forces of plate motion. *Geophysical Journal International*, *43*(1), 163–200. https://doi.org/10.1111/j.1365-246x.1975.tb00631.x
Fukao, Y., & Obayashi, M. (2013). Subducted slabs stagnant above, penetrating through, and trapped below the 660 km discontinuity. *Journal of Geophysical Research: Solid Earth*, *118*(11), 5920–5938. https://doi.org/10.1002/2013jb010466
Funiciello, F., Faccenna, C., & Giardini, D. (2004). Role of lateral mantle flow in the evolution of subduction systems: Insights from laboratory experiments. *Geophysical Journal International*, *157*(3), 1393–1406. https://doi.org/10.1111/j.1365-246x.2004.02313.x
Funiciello, F., Faccenna, C., Giardini, D., & Regenauer-Lieb, K. (2003). Dynamics of retreating slabs: 2. Insights from three-dimensional laboratory experiments. *Journal of Geophysical Research*, *108*(B4), 2207. https://doi.org/10.1029/2001jb000896
Funiciello, F., Faccenna, C., Heuret, A., Lallemand, S., Di Giuseppe, E., & Becker, T. W. (2008). Trench migration, net rotation and slab–mantle coupling. *Earth and Planetary Science Letters*, *271*(1–4), 233–240. https://doi.org/10.1016/j.epsl.2008.04.006
Funiciello, F., Morra, G., Regenauer-Lieb, K., & Giardini, D. (2003). Dynamics of retreating slabs: 1. Insights from two-dimensional numerical experiments. *Journal of Geophysical Research*, *108*(B4), 2206. https://doi.org/10.1029/2001jb000898
Ghosh, A., Thyagarajulu, G., & Steinberger, B. (2017). The importance of upper mantle heterogeneity in generating the Indian Ocean geoid low. *Geophysical Research Letters*, *44*(19), 9707–9715. https://doi.org/10.1002/2017GL075392
Goldberg, S. L., & Holt, A. F. (2023). Characterizing the complexity of subduction zone flow with an ensemble of multiscale global convection models [Dataset]. Geochemistry, Geophysics, Geosystems. Zenodo. https://doi.org/10.5281/zenodo.10143376
Gripp, A. E., & Gordon, R. G. (2002). Young tracks of hotspots and current plate velocities. *Geophysical Journal International*, *150*(2), 321–361. https://doi.org/10.1046/j.1365-246x.2002.01627.x
Hager, B. H. (1984). Subducted slabs and the geoid: Constraints on mantle rheology and flow. *Journal of Geophysical Research*, *89*(B7), 6003–6015. https://doi.org/10.1029/jb089ib07p06003
Hager, B. H., Clayton, R. W., Richards, M. A., Comer, R. P., & Dziewonski, A. M. (1985). Lower mantle heterogeneity, dynamic topography and the geoid. *Nature*, *313*(6003), 541–545. https://doi.org/10.1038/313541a0
Hager, B. H., & O'Connell, R. J. (1978). Subduction zone dip angles and flow driven by plate motion. *Tectonophysics*, *50*(2–3), 111–133. https://doi.org/10.1016/0040-1951(78)90130-0
Hager, B. H., & O'Connell, R. J. (1979). Kinematic models of large-scale flow in the Earth's mantle. *Journal of Geophysical Research*, *84*(B3), 1031–1048. https://doi.org/10.1029/jb084ib03p01031
Hager, B. H., & O'Connell, R. J. (1981). A simple global model of plate dynamics and mantle convection. *Journal of Geophysical Research*, *86*(B6), 4843–4867. https://doi.org/10.1029/jb086ib06p04843
Hager, B. H., & Richards, M. A. (1989). Long-wavelength variations in Earth's geoid: Physical models and dynamical implications. *Philosophical Transactions of the Royal Society of London. Series A, Mathematical and Physical Sciences*, *328*(1599), 309–327. https://doi.org/10.1098/rsta.1989.0038
Haskell, N. A. (1935). The motion of a viscous fluid under a surface load. *Physics*, *6*(8), 265–269. https://doi.org/10.1063/1.1745329
Hayes, G. P., Moore, G. L., Portner, D. E., Hearne, M., Flamme, H., Furtney, M., & Smoczyk, G. M. (2018). Slab2, a comprehensive subduction zone geometry model. *Science*, *362*(6410), 58–61. https://doi.org/10.1126/science.aat4723
Heister, T., Dannberg, J., Gassmöller, R., & Bangerth, W. (2017). High accuracy mantle convection simulation through modern numerical methods - II: Realistic models and problems. *Geophysical Journal International*, *210*(2), 833–851. https://doi.org/10.1093/gji/ggx195
Hirth, G., & Kohlstedt, D. (2003). Rheology of the upper mantle and the mantle wedge: A view from the experimentalists. *Geophysical Monograph - American Geophysical Union*, *138*, 83–106.
Holt, A. F. (2022). The topographic signature of mantle pressure build-up beneath subducting plates: A numerical modeling study. *Geophysical Research Letters*, *49*(22), e2022GL100330. https://doi.org/10.1029/2022GL100330
Holt, A. F., & Becker, T. W. (2017). The effect of a power-law mantle viscosity on trench retreat rate. *Geophysical Journal International*, *208*(1), 491–507. https://doi.org/10.1093/gji/ggw392
Holt, A. F., & Royden, L. H. (2020). Subduction dynamics and mantle pressure: 2. Towards a global understanding of slab dip and upper mantle circulation. *Geochemistry, Geophysics, Geosystems*, *21*(7), e2019GC008771. https://doi.org/10.1029/2019gc008771
Holt, A. F., Royden, L. H., & Becker, T. W. (2017). The dynamics of double slab subduction. *Geophysical Journal International*, *209*(1), 250–265. https://doi.org/10.1093/gji/ggw496
Holt, A. F., Royden, L. H., Becker, T. W., & Faccenna, C. (2018). Slab interactions in 3-D subduction settings: The Philippine Sea Plate region. *Earth and Planetary Science Letters*, *489*, 72–83. https://doi.org/10.1016/j.epsl.2018.02.024

Holt, W. E. (1995). Flow fields within the Tonga slab determined from the moment tensors of deep earthquakes. *Geophysical Research Letters*, *22*(8), 989–992. https://doi.org/10.1029/95gl00786
Hu, J., Gurnis, M., Rudi, J., Stadler, G., & Müller, R. D. (2022). Dynamics of the abrupt change in Pacific Plate motion around 50 million years ago. *Nature Geoscience*, *15*(1), 74–78. https://doi.org/10.1038/s41561-021-00862-6
Husson, L. (2012). Trench migration and upper plate strain over a convecting mantle. *Physics of the Earth and Planetary Interiors*, *212*, 32–43. https://doi.org/10.1016/j.pepi.2012.09.006
Husson, L., Conrad, C. P., & Faccenna, C. (2008). Tethyan closure, Andean orogeny, and westward drift of the Pacific Basin. *Earth and Planetary Science Letters*, *271*(1–4), 303–310. https://doi.org/10.1016/j.epsl.2008.04.022
Husson, L., Conrad, C. P., & Faccenna, C. (2012). Plate motions, Andean orogeny, and volcanism above the South Atlantic convection cell. *Earth and Planetary Science Letters*, *317*, 126–135. https://doi.org/10.1016/j.epsl.2011.11.040
Husson, L., Guillaume, B., Funiciello, F., Faccenna, C., & Royden, L. H. (2012). Unraveling topography around subduction zones from laboratory models. *Tectonophysics*, *526*, 5–15. https://doi.org/10.1016/j.tecto.2011.09.001
Jadamec, M. A., & Billen, M. I. (2010). Reconciling surface plate motions with rapid three-dimensional mantle flow around a slab edge. *Nature*, *465*(7296), 338–341. https://doi.org/10.1038/nature09053
Jadamec, M. A., & Billen, M. I. (2012). The role of rheology and slab shape on rapid mantle flow: Three-dimensional numerical models of the Alaska slab edge. *Journal of Geophysical Research*, *117*(B2), B02304. https://doi.org/10.1029/2011jb008563
Jagoutz, O., Royden, L., Holt, A. F., & Becker, T. W. (2015). Anomalously fast convergence of India and Eurasia caused by double subduction. *Nature Geoscience*, *8*(6), 475–478. https://doi.org/10.1038/NGEO2418
Karato, S., & Wu, P. (1993). Rheology of the upper mantle: A synthesis. *Science*, *260*(5109), 771–778. https://doi.org/10.1126/science.260.5109.771
Kincaid, C., & Griffiths, R. W. (2003). Laboratory models of the thermal evolution of the mantle during rollback subduction. *Nature*, *425*(6953), 58–62. https://doi.org/10.1038/nature01923
Király, Á., Capitanio, F. A., Funiciello, F., & Faccenna, C. (2016). Subduction zone interaction: Controls on arcuate belts. *Geology*, *44*(9), 715–718. https://doi.org/10.1130/g37912.1
Király, Á., Capitanio, F. A., Funiciello, F., & Faccenna, C. (2017). Subduction induced mantle flow: Length-scales and orientation of the toroidal cell. *Earth and Planetary Science Letters*, *479*, 284–297. https://doi.org/10.1016/j.epsl.2017.09.017
Kronbichler, M., Heister, T., & Bangerth, W. (2012). High accuracy mantle convection simulation through modern numerical methods. *Geophysical Journal International*, *191*(1), 12–29. https://doi.org/10.1111/j.1365-246X.2012.05609.x
Lau, H. C. P., Mitrovica, J. X., Austermann, J., Crawford, O., Al-Attar, D., & Latychev, K. (2016). Inferences of mantle viscosity based on ice age data sets: Radial structure. *Journal of Geophysical Research: Solid Earth*, *121*(10), 6991–7012. https://doi.org/10.1002/2016jb013043
Lemoine, F. G., Kenyon, S. C., Factor, J. K., Trimmer, R. G., Pavlis, N. K., Chinn, D. S., et al. (1998). The development of the joint NASA GSFC and the National Imagery and Mapping Agency (NIMA) geopotential model EGM96.
Li, C., van der Hilst, R. D., Engdahl, E. R., & Burdick, S. (2008). A new global model for P wave speed variations in Earth's mantle. *Geochemistry, Geophysics, Geosystems*, *9*(5), Q05018. https://doi.org/10.1029/2007gc001806
Lithgow-Bertelloni, C., & Richards, M. A. (1998). The dynamics of Cenozoic and Mesozoic plate motions. *Reviews of Geophysics*, *36*(1), 27–78. https://doi.org/10.1029/97rg02282
Liu, S., & King, S. D. (2019). A benchmark study of incompressible Stokes flow in a 3-D spherical shell using ASPECT. *Geophysical Journal International*, *217*(1), 650–667. https://doi.org/10.1093/gji/ggz036
Liu, X., Zhao, D., Li, S., & Wei, W. (2017). Age of the subducting Pacific slab beneath East Asia and its geodynamic implications. *Earth and Planetary Science Letters*, *464*, 166–174. https://doi.org/10.1016/j.epsl.2017.02.024
Long, M. D. (2013). Constraints on subduction geodynamics from seismic anisotropy. *Reviews of Geophysics*, *51*(1), 76–112. https://doi.org/10.1002/rog.20008
Long, M. D., & Silver, P. G. (2008). The subduction zone flow field from seismic anisotropy: A global view. *Science*, *319*(5861), 315–318. https://doi.org/10.1126/science.1150809
Lu, C., Grand, S. P., Lai, H., & Garnero, E. J. (2019). TX2019slab: A new P and S tomography model incorporating subducting slabs. *Journal of Geophysical Research: Solid Earth*, *124*(11), 11549–11567. https://doi.org/10.1029/2019JB017448
Lynner, C., & Long, M. D. (2014). Testing models of sub-slab anisotropy using a global compilation of source-side shear wave splitting data. *Journal of Geophysical Research: Solid Earth*, *119*(9), 7226–7244. https://doi.org/10.1002/2014jb010983
Manea, V. C., Pérez-Gussinyé, M., & Manea, M. (2012). Chilean flat slab subduction controlled by overriding plate thickness and trench rollback. *Geology*, *40*(1), 35–38. https://doi.org/10.1130/g32543.1
McKenzie, D. P. (1969). Speculations on the consequences and causes of plate motions. *Geophysical Journal International*, *18*(1), 1–32. https://doi.org/10.1111/j.1365-246x.1969.tb00259.x
Mitrovica, J. X., & Forte, A. M. (2004). A new inference of mantle viscosity based upon joint inversion of convection and glacial isostatic adjustment data. *Earth and Planetary Science Letters*, *225*(1–2), 177–189. https://doi.org/10.1016/j.epsl.2004.06.005
Moresi, L., & Gurnis, M. (1996). Constraints on the lateral strength of slabs from three-dimensional dynamic flow models. *Earth and Planetary Science Letters*, *138*(1–4), 15–28. https://doi.org/10.1016/0012-821x(95)00221-w
Nicolas, A., & Christensen, N. I. (1987). Formation of anisotropy in upper mantle peridotites-A review. *Composition, Structure and Dynamics of the Lithosphere-asthenosphere System*, *16*, 111–123.
O'Driscoll, L. J., Richards, M. A., & Humphreys, E. D. (2012). Nazca–South America interactions and the late Eocene–late Oligocene flat-slab episode in the central Andes. *Tectonics*, *31*(2), TC2013. https://doi.org/10.1029/2011tc003036
Osei Tutu, A., Sobolev, S. V., Steinberger, B., Popov, A. A., & Rogozhina, I. (2018). Evaluating the influence of plate boundary friction and mantle viscosity on plate velocities. *Geochemistry, Geophysics, Geosystems*, *19*(3), 642–666. https://doi.org/10.1002/2017gc007112
Paczkowski, K., Montési, L. G. J., Long, M. D., & Thissen, C. J. (2014). Three-dimensional flow in the subslab mantle. *Geochemistry, Geophysics, Geosystems*, *15*(10), 3989–4008. https://doi.org/10.1002/2014gc005441
Paczkowski, K., Thissen, C. J., Long, M. D., & Montési, L. G. J. (2014). Deflection of mantle flow beneath subducting slabs and the origin of subslab anisotropy. *Geophysical Research Letters*, *41*(19), 6734–6742. https://doi.org/10.1002/2014gl060914
Pekeris, C. L. (1935). Thermal convection in the interior of the Earth. *Geophysical Journal International*, *3*, 343–367. https://doi.org/10.1111/j.1365-246x.1935.tb01742.x
Peral, M., Király, Á., Zlotnik, S., Funiciello, F., Fernàndez, M., Faccenna, C., & Vergés, J. (2018). Opposite subduction polarity in adjacent plate segments. *Tectonics*, *37*(9), 3285–3302. https://doi.org/10.1029/2017tc004896
Piromallo, C., Becker, T. W., Funiciello, F., & Faccenna, C. (2006). Three-dimensional instantaneous mantle flow induced by subduction. *Geophysical Research Letters*, *33*(8), 5–8. https://doi.org/10.1029/2005GL025390

Ricard, Y., Richards, M., Lithgow-Bertelloni, C., & le Stunff, Y. (1993). A geodynamic model of mantle density heterogeneity. *Journal of Geophysical Research*, *98*(B12), 21895–21909. https://doi.org/10.1029/93jb02216

Ricard, Y., & Vigny, C. (1989). Mantle dynamics with induced plate tectonics. *Journal of Geophysical Research*, *94*(B12), 17543–17559. https://doi.org/10.1029/jb094ib12p17543

Royden, L. H., & Holt, A. F. (2020). Subduction dynamics and mantle pressure: 1. An analytical framework relating subduction geometry, Plate motion, and asthenospheric pressure. *Geochemistry, Geophysics, Geosystems*, *21*(7), e2020GC009032. https://doi.org/10.1029/2020gc009032

Royden, L. H., & Husson, L. (2006). Trench motion, slab geometry and viscous stresses in subduction systems. *Geophysical Journal International*, *167*(2), 881–905. https://doi.org/10.1111/j.1365-246x.2006.03079.x

Russo, R. M., & Silver, P. G. (1994). Trench-parallel flow beneath the Nazca plate from seismic anisotropy. *Science*, *263*(5150), 1105–1111. https://doi.org/10.1126/science.263.5150.1105

Saxena, A., Dannberg, J., Gassmöller, R., Fraters, M., Heister, T., & Styron, R. (2023). High-resolution mantle flow models reveal importance of plate boundary geometry and slab pull forces on generating tectonic plate motions. *Journal of Geophysical Research: Solid Earth*, *128*(8), e2022JB025877. https://doi.org/10.1029/2022jb025877

Schaeffer, A. J., & Lebedev, S. (2015). Global heterogeneity of the lithosphere and underlying mantle: A seismological appraisal based on multimode surface-wave dispersion analysis, shear-velocity tomography, and tectonic regionalization. *The Earth's Heterogeneous Mantle: A Geophysical, Geodynamical, and Geochemical Perspective*, 3–46.

Schellart, W. P., Freeman, J., Stegman, D. R., Moresi, L., & May, D. (2007). Evolution and diversity of subduction zones controlled by slab width. *Nature*, *446*(7133), 308–311. https://doi.org/10.1038/nature05615

Schepers, G., Van Hinsbergen, D. J. J., Spakman, W., Kosters, M. E., Boschman, L. M., & McQuarrie, N. (2017). South-American plate advance and forced Andean trench retreat as drivers for transient flat subduction episodes. *Nature Communications*, *8*(1), 15249. https://doi.org/10.1038/ncomms15249

Schubert, G., & Turcotte, D. L. (1972). One-dimensional model of shallow-mantle convection. *Journal of Geophysical Research*, *77*(5), 945–951. https://doi.org/10.1029/JB077i005p00945

Schubert, G., Yuen, D. A., Froidevaux, C., Fleitout, L., & Souriau, M. (1978). Mantle circulation with partial shallow return flow: Effects on stresses in oceanic plates and topography of the sea floor. *Journal of Geophysical Research*, *83*(B2), 745–758. https://doi.org/10.1029/JB083iB02p00745

Semple, A. G., & Lenardic, A. (2021). Feedbacks between a non-Newtonian upper mantle, mantle viscosity structure and mantle dynamics. *Geophysical Journal International*, *224*(2), 961–972. https://doi.org/10.1093/gji/ggaa495

Spasojevic, S., Gurnis, M., & Sutherland, R. (2010). Mantle upwellings above slab graveyards linked to the global geoid lows. *Nature Geoscience*, *3*(6), 435–438. https://doi.org/10.1038/ngeo855

Stadler, G., Gurnis, M., Burstedde, C., Wilcox, L. C., Alisic, L., & Ghattas, O. (2010). The dynamics of plate tectonics and mantle flow: From local to global scales. *Science*, *329*(5995), 1033–1038. https://doi.org/10.1126/science.1191223

Stegman, D. R., Freeman, J., Schellart, W. P., Moresi, L., & May, D. (2006). Influence of trench width on subduction hinge retreat rates in 3-D models of slab rollback. *Geochemistry, Geophysics, Geosystems*, *7*(3), Q03012. https://doi.org/10.1029/2005gc001056

Steinberger, B. (2000). Slabs in the lower mantle — Results of dynamic modelling compared with tomographic images and the geoid. *Physics of the Earth and Planetary Interiors*, *118*(3–4), 241–257. https://doi.org/10.1016/S0031-9201(99)00172-7

Steinberger, B. (2016). Topography caused by mantle density variations: Observation-based estimates and models derived from tomography and lithosphere thickness. *Geophysical Journal International*, *205*(1), 604–621. https://doi.org/10.1093/gji/ggw040

Steinberger, B., & Becker, T. W. (2018). A comparison of lithospheric thickness models. *Tectonophysics*, *746*, 325–338. https://doi.org/10.1016/j.tecto.2016.08.001

Steinberger, B., & Calderwood, A. R. (2006). Models of large-scale viscous flow in the Earth's mantle with constraints from mineral physics and surface observations. *Geophysical Journal International*, *167*(3), 1461–1481. https://doi.org/10.1111/j.1365-246X.2006.03131.x

Steinberger, B., Rathnayake, S., & Kendall, E. (2021). The Indian Ocean geoid low at a plume-slab overpass. *Tectonophysics*, *817*, 229037. https://doi.org/10.1016/j.tecto.2021.229037

Stern, R. J. (2002). Subduction zones. *Reviews of Geophysics*, *40*(4), 3-1–3-38. https://doi.org/10.1029/2001rg000108

Stevenson, D. J., & Turner, J. S. (1977). Angle of subduction. *Nature*, *270*(5635), 334–336. https://doi.org/10.1038/270334a0

Tovish, A., Schubert, G., & Luyendyk, B. P. (1978). Mantle flow pressure and the angle of subduction: Non-Newtonian corner flows. *Journal of Geophysical Research*, *83*(B12), 5892–5898. https://doi.org/10.1029/jb083ib12p05892

Turcotte, D. L., & Schubert, G. (2014). *Geodynamics*. Cambridge University Press.

van der Hilst, R. D., Widiyantoro, S., & Engdahl, E. R. (1997). Evidence for deep mantle circulation from global tomography. *Nature*, *386*(6625), 578–584. https://doi.org/10.1038/386578a0

Walpole, J., Wookey, J., Kendall, J. M., & Masters, T. G. (2017). Seismic anisotropy and mantle flow below subducting slabs. *Earth and Planetary Science Letters*, *465*, 155–167. https://doi.org/10.1016/j.epsl.2017.02.023

White, D. A., Roeder, D. H., Nelson, T. H., & Crowell, J. C. (1970). Subduction. *Geological Society of America Bulletin*, *81*(11), 3431–3432. https://doi.org/10.1130/0016-7606(1970)81[3431:s]2.0.co;2

Wu, B., Conrad, C. P., Heuret, A., Lithgow-Bertelloni, C., & Lallemand, S. (2008). Reconciling strong slab pull and weak plate bending: The plate motion constraint on the strength of mantle slabs. *Earth and Planetary Science Letters*, *272*(1–2), 412–421. https://doi.org/10.1016/j.epsl.2008.05.009